

IDOL regulates systemic energy balance through control of neuronal VLDLR expression

Stephen D. Lee^{1,9}, Christina Priest^{1,9}, Mikael Bjursell², Jie Gao¹, Douglas V. Arneson³, In Sook Ahn³, Graciela Diamante³, J. Edward van Veen³, Megan G. Massa^{1,9}, Anna C. Calkin¹, Jason Kim¹, Harriet Andersén², Prashant Rajbhandari¹, Michelle Porritt², Alba Carreras², Andrea Ahnmark⁴, Frank Seeliger⁵, Ingela Maxvall⁴, Pernilla Eliasson⁴, Magnus Althage⁴, Peter Åkerblad⁴, Daniel Lindén^{4,6}, Tracy A. Cole⁷, Richard Lee⁷, Helen Boyd⁸, Mohammad Bohlooly-Y², Stephanie M. Correa³, Xia Yang^{1,9}, Peter Tontonoz^{1,9*} and Cynthia Hong¹

Liver X receptors limit cellular lipid uptake by stimulating the transcription of inducible degrader of the low-density lipoprotein receptor (IDOL), an E3 ubiquitin ligase that targets lipoprotein receptors for degradation. The function of IDOL in systemic metabolism is incompletely understood. Here we show that loss of IDOL in mice protects against the development of diet-induced obesity and metabolic dysfunction by altering food intake and thermogenesis. Unexpectedly, analysis of tissue-specific knockout mice revealed that IDOL affects energy balance, not through its actions in peripheral metabolic tissues (liver, adipose tissue, endothelium, intestine, and skeletal muscle) but by controlling lipoprotein receptor abundance in neurons. Single-cell RNA sequencing of the hypothalamus demonstrated that IDOL deletion altered gene expression linked to the control of metabolism. Finally, we identified very low-density lipoprotein receptor (VLDLR) rather than low-density lipoprotein receptor (LDLR) as the primary mediator of the effects of IDOL on energy balance. These data identify a role for the neuronal IDOL-VLDLR pathway in metabolic homoeostasis and diet-induced obesity.

Lipoprotein receptors are key determinants of cardiovascular disease owing to their pivotal roles in regulating blood cholesterol levels. Assessment of the function and regulation of members of the low-density lipoprotein receptor (LDLR) superfamily has advanced our understanding of fundamental processes such as receptor-mediated endocytosis¹, neuronal development², and lipid-responsive transcription³. Cells maintain optimal cholesterol levels, in part by regulating the uptake of cholesterol from circulating lipoproteins via LDLR. Sterol regulatory element binding proteins (SREBPs) are transcription factors that are activated by low cholesterol levels and stimulate the expression of genes that drive cholesterol synthesis and uptake, including LDLR. Conversely, when cells accumulate excess cholesterol, activation of the liver X receptors (LXRs) promotes the expression of genes that restore homoeostasis by increasing cholesterol efflux and transport^{4,5}. The LXR and SREBP pathways also exert negative feedback on each other^{6,7}.

One LXR-mediated feedback mechanism is to limit the influx of lipoprotein cholesterol into cells via the inducible degrader of the LDLR (IDOL), an E3 ubiquitin ligase that targets members of the LDLR family for degradation^{8,9}. Previous work elucidated the molecular mechanisms underlying IDOL-dependent degradation of its lipoprotein receptor targets^{9–13} and addressed its role in the species-specific regulation of hepatic cholesterol metabolism^{14–18}. IDOL and its targets are expressed in a number of metabolically

active tissues other than the liver, but the physiological role of IDOL in systemic lipid metabolism remains poorly understood. Furthermore, the lipoprotein receptor (or receptors) through which IDOL regulates metabolism are unknown.

Here we report that mice globally deficient in IDOL expression are protected against diet-induced obesity and metabolic dysfunction. Unexpectedly, loss of IDOL in individual metabolic tissues, including the liver, skeletal muscle, adipose tissue, and intestine, failed to recapitulate the phenotype of the whole-body knockouts, prompting us to search for an alternative mechanism. Ultimately, we traced this metabolic phenotype to loss of IDOL in the central nervous system (CNS), and to the consequent dysregulation of VLDLR protein levels. Deletion of IDOL from mouse neurons mimics the phenotype of the whole-body IDOL knockout mice. Our data identify the IDOL–VLDLR axis in neurons as a regulatory pathway that affects systemic energy balance.

Results

Global IDOL knockout mice are protected from diet-induced metabolic dysfunction. Previous efforts to characterize the physiological role of IDOL have focused primarily on its ability to regulate cholesterol metabolism. Unexpectedly, in the course of these studies, we noted that 18-month-old chow-fed IDOL knockout mice (developed at the University of California, Los Angeles (UCLA),

¹Department of Pathology and Laboratory Medicine, Department of Biological Chemistry, and Molecular Biology Institute, David Geffen School of Medicine, University of California, Los Angeles, Los Angeles, CA, USA. ²Discovery Sciences, BioPharmaceuticals R&D, AstraZeneca, Gothenburg, Sweden.

³Department of Integrative Biology and Physiology, University of California, Los Angeles, Los Angeles, CA, USA. ⁴Research and Early Development Cardiovascular, Renal and Metabolism, BioPharmaceuticals R&D, AstraZeneca, Gothenburg, Sweden. ⁵Pathology, Clinical Pharmacology and Safety Sciences, R&D, AstraZeneca, Gothenburg, Sweden. ⁶Division of Endocrinology, Department of Neuroscience and Physiology, Sahlgrenska Academy, University of Gothenburg, Gothenburg, Sweden. ⁷Central Nervous System Group, Antisense Drug Discovery, Ionis Pharmaceuticals, Inc, Carlsbad, CA, USA. ⁸Clinical Pharmacology and Safety Sciences, R&D, AstraZeneca; Cambridge Science Park, Cambridge, UK. ⁹These authors contributed equally: Stephen D. Lee, Christina Priest. *e-mail: PTontonoz@mednet.ucla.edu

USA) demonstrated that deletion of IDOL protected against age-induced obesity, even when the mice were fed a standard chow diet (Extended Data Fig. 1a,b). We then proceeded to challenge mice with obesogenic diets. Group-housed IDOL knockout mice fed a western diet enriched in fat and cholesterol for 15 weeks were 22% lighter than wild-type controls (Fig. 1a). Body composition analysis by magnetic resonance imaging (MRI) revealed that IDOL knockout mice were leaner, averaging 11% body fat compared to 32% in wild-type mice (Fig. 1b). This was accompanied by reduced hepatic lipid accumulation and smaller adipocytes in the inguinal white adipose tissue depot (Fig. 1c). As the gene encoding IDOL is an LXR target, we postulated that the differential response to diet may require dietary cholesterol to stimulate LXR activity; however, the IDOL knockout mice were also leaner when fed a high-fat diet (HFD) that contained comparatively little cholesterol (Extended Data Fig. 1c).

We also analysed a second, independently derived IDOL knockout mouse line generated by crossing *Idol*-floxed mice developed at AstraZeneca, denoted IDOL(AZ), with a Rosa26-Cre transgenic line, denoted *Cre*^{R26} (Supplementary Fig. 1). When maintained on a low-fat, low-cholesterol diet (LFD), these *Cre*^{R26}/*Idol*^{fl/fl} mice also showed a lean phenotype after 20 weeks of age (Extended Data Fig. 1d). The phenotype was exaggerated when the mice were challenged with a high-fat, high-cholesterol (HFHC) diet (Extended Data Fig. 1e).

We found no evidence of a generalized developmental growth defect in either strain of IDOL knockout mice. There were no differences in lean body mass (Extended Data Fig. 1f), nasal to anal length (Extended Data Fig. 1g), or body temperature attributable to genotype (Extended Data Fig. 1h). The reduced adiposity in the western diet-fed IDOL knockout mice was associated with improved glucose clearance (Fig. 1d, 9 weeks of western diet) and insulin tolerance (Fig. 1e, 14 weeks of western diet). Although we did not detect differences in food intake in the short term (<7 d), analysis of mice housed singly over the course of weeks (wild type, $n=14$; IDOL knockout, $n=12$) revealed reduced food intake in the genetic absence of IDOL (Fig. 1f), associated with reduced diet-induced adipose expansion (Fig. 1g,h).

Deletion of IDOL from peripheral metabolic tissues does not protect against obesity. We postulated that the metabolic phenotype of IDOL-deficient mice resulted from the primary actions of the IDOL pathway in one or more metabolic tissues. To test this idea, we crossed *Idol*-floxed mice to a range of tissue-specific *Cre* transgenic mouse lines to generate tissue-selective IDOL knockouts. We first analysed the contribution of the liver to the IDOL knockout phenotype using *Alb*-*Cre*-IDOL(AZ)-floxed mice (*Idol*(AZ)^{fl/fl}; *Cre*^{Alb}) generated at AstraZeneca. Hepatic deletion of IDOL had no effect on the obesity of mice challenged with the obesogenic HFHC diet (Fig. 2a,f), nor on glucose metabolism (Extended Data Fig. 2a,b), suggesting that the liver is not the primary driver of the global IDOL knockout phenotype.

Given the reduced adiposity in IDOL knockout mice, we next considered that a direct effect of the IDOL pathway on adipose tissue might explain the phenotype. We crossed *AdipoQ*-*Cre* transgenic mice¹⁹ to *Idol*^{fl/fl} mice to generate mice lacking IDOL expression in both white and brown fat (*Idol*^{fl/fl}; *Cre*^{AdipoQ}). We challenged the mice with 15 weeks of western-diet feeding but saw no effect on mass or adiposity (Fig. 2b,g), or on glucose or insulin tolerance (Extended Data Fig. 2c,d). In a complementary approach, we developed a transgenic mouse expressing a dominant active form of human IDOL under the control of the *Fabp4* promoter (aP2-Tg). This line showed nearly complete ablation of VLDLR protein levels in both white and brown adipose depots, confirming the activation of the IDOL pathway (Extended Data Fig. 3a,b). Despite this change in VLDLR levels, we observed no differences in mass between the

aP2-IDOL Tg mice and their littermate controls fed a western diet for 12 weeks (Extended Data Fig. 3c). Accordingly, neither adiposity nor responses to glucose or insulin challenges were affected by the transgene (Extended Data Fig. 3d-f). Collectively the data collected from both gain-of-function and loss-of-function mice lead us to conclude that adipose-intrinsic actions of IDOL cannot explain the phenotype of global IDOL knockout mice.

We next considered the possibility that IDOL-dependent changes in LDLR or VLDLR protein levels may act in the vasculature to alter lipid delivery and metabolism in adipocytes secondarily. This would be consistent with studies showing that VLDLR affects lipoprotein lipase activity^{20–23}. We crossed *Idol*^{fl/fl} mice with a line expressing Cre from the cadherin 5 promoter (commonly referred to as VE cadherin-Cre)²⁴ to generate an endothelial-specific IDOL knockout line (*Idol*^{fl/fl}; *Cre*^{Cdh5}). Loss of IDOL activity in the endothelium had no effect on the initiation or progression of obesity after challenge with a western diet for 15 weeks (Fig. 2c,h). There was also no difference in glucose or insulin tolerance between groups (Extended Data Fig. 2e,f).

An alternative possibility was that altered caloric intake from the diet could cause the change in weight gain. *Idol* is highly expressed in the intestine⁸, and it is plausible that altering lipoprotein receptor expression could affect dietary lipid absorption or efflux. We crossed the *Idol*-floxed mice with *Villin*-*Cre* transgenic mice to generate intestine-specific knockout mice (*Idol*^{fl/fl}; *Cre*^{Vil}). However, loss of IDOL activity in the intestine did not affect mass gain or adiposity (Fig. 2d,i) and did not affect glucose or insulin tolerance (Extended Data Fig. 2g,h). Prompted by the high level of expression of *Vldlr* in muscle, we also generated muscle-specific IDOL knockouts (*Idol*^{fl/fl}; *Cre*^{Mck}) by crossing the *Idol*-floxed mice to MCK-Cre transgenic mice²⁵. Again, the tissue-selective knockout failed to recapitulate the effects of whole-body IDOL loss (Fig. 2e,j and Extended Data Fig. 2i,j).

IDOL regulates systemic energy balance through VLDLR. IDOL controls the abundance of three proteins (LDLR, VLDLR, and ApoER2) via ubiquitination, which targets the proteins for lysosomal degradation^{9,13}. We therefore postulated that the metabolic phenotype of the global IDOL knockout was due to changes in levels of one or more of these lipoprotein receptors. To test this idea, we developed two double-knockout mouse lines in which IDOL and either LDLR or VLDLR were deleted simultaneously. We did not pursue an ApoER2 compound mutant line as global ApoER2 knockout mice are sterile²⁶ and have severe neurological defects at baseline², and floxed-Apoer2 mice are not available. We challenged cohorts of single and double IDOL knockout mice with a HFHC diet. Consistent with the results of prior cohorts, the mass (Fig. 3a,b) and adiposity (Fig. 3e,f) of global IDOL knockout mice diverged rapidly from the wild-type group, reaching statistical significance after 2–4 weeks on the HFHC diet ($P<0.05$ by repeat measures two-way ANOVA). Throughout the study, the IDOL knockout and IDOL-LDLR double-knockout groups were indistinguishable with respect to body mass and adiposity (Fig. 3a,e). LDLR is the only IDOL target expressed in the liver, further supporting the conclusion that the liver is not the primary driver of the global IDOL knockout phenotype.

Whole-body deletion of VLDLR has previously been shown to be protective against diet-induced obesity^{22,27,28}. To further understand the contributions of IDOL to body weight we compared the responses of wild-type, VLDLR knockout, IDOL knockout, and IDOL-VLDLR double-knockout mice to HFHC diet feeding (Fig. 3b,f). The VLDLR single-knockout mice and IDOL-VLDLR double-knockout mice showed comparable protection against adipose expansion following HFD feeding, confirming previous reports that deletion of VLDLR is protective against diet-induced obesity. We further showed that deletion of IDOL, which leads to an

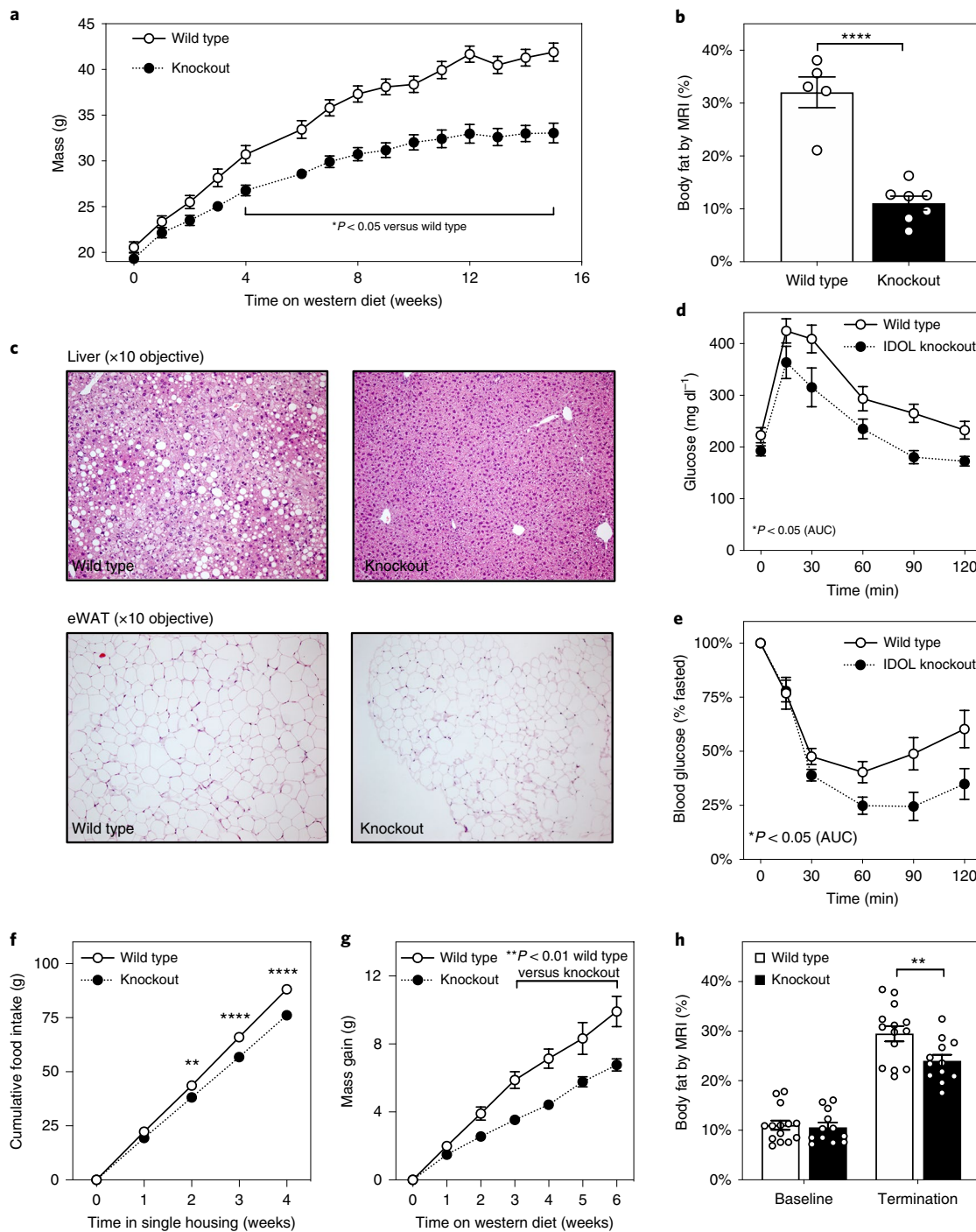


Fig. 1 | Global IDOL knockout mice are protected from diet-induced metabolic dysfunction. **a**, Growth curve for wild-type versus IDOL knockout (KO) mice fed a western diet from 5–6 weeks of age. The mean masses are shown \pm the s.e.m., $n=12$ wild-type mice, $n=9$ knockout mice. * $P<0.05$ by repeat measures two-way ANOVA. **b**, Adiposity reported as body fat percentage \pm the s.e.m., as measured by MRI after 15 weeks of western diet feeding. $n=5$ wild-type mice, $n=7$ knockout mice. **** $P<0.0001$ by two-tailed t-test. **c**, Haematoxylin- and eosin-stained sections of liver and epididymal white adipose tissue (eWAT) depots from mice maintained on a western diet for 15 weeks; these images are representative of tissues analysed from both the UCLA-produced and AstraZeneca-produced lines. **d**, Intraperitoneal glucose tolerance test (1mg kg^{-1}) administered after 9 weeks of western diet feeding. The mean blood glucose levels are shown \pm the s.e.m., $n=10$ wild-type mice, $n=9$ knockout mice. * $P<0.05$ by two-tailed t-test of the AUC. **e**, Intraperitoneal insulin tolerance test (1U kg^{-1}) administered after 14 weeks of western diet feeding. The mean blood glucose levels are shown \pm s.e.m. $n=7$ wild-type mice, $n=6$ knockout mice. * $P<0.05$ by two-tailed t-test of the AUC. **f**, The mean food consumed per mouse is labelled \pm s.e.m. **g**, The mean mass gained per mouse after being placed in single housing \pm s.e.m. **h**, Adiposity reported as body fat percentage \pm s.e.m., as measured by MRI. The precise n , P values, and details of the statistical testing are provided in the source data file.

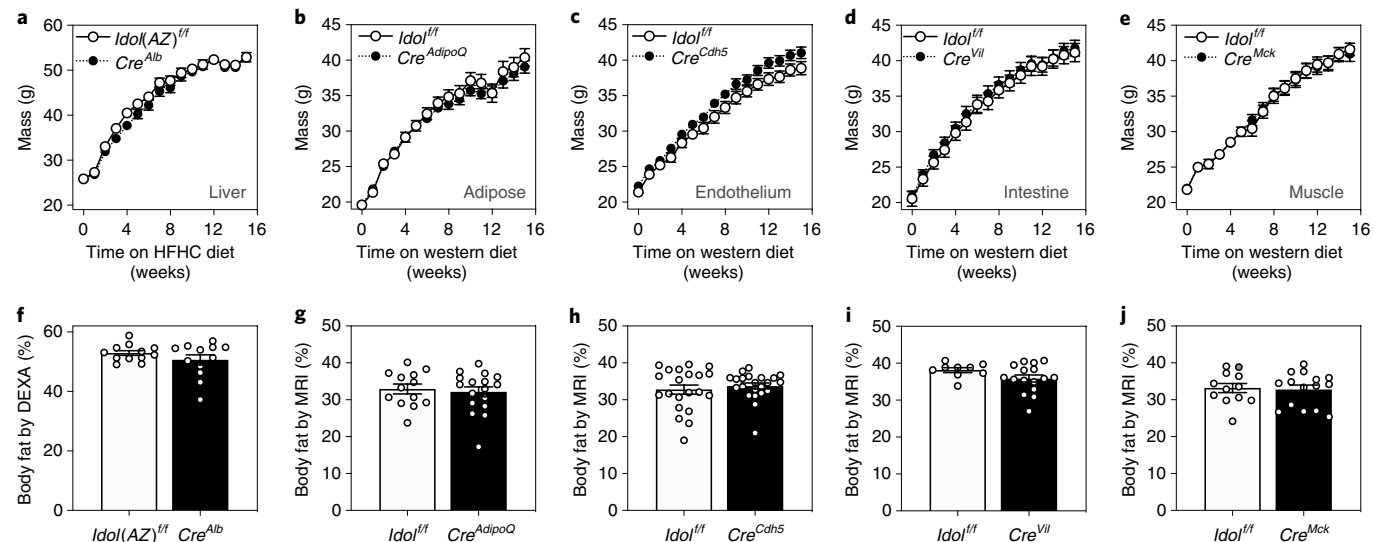


Fig. 2 | Deletion of IDOL from peripheral tissues does not protect against diet-induced metabolic dysfunction. **a–e**, Growth curves showing the mean mass \pm s.e.m. for male mice from each conditional knockout mouse strain tested. **f–j**, Adiposity reported as body fat percentage \pm s.e.m. measured by MRI or DEXA after 15 weeks of consuming the indicated test diet. **a,f**, Liver-specific IDOL knockout mice ($n=12$ *Idol^{AZ}*/*Idol^{AZ}*, $n=12$ *Idol^{AZ}*/*Cre^{Alb}*) fed a HFHC diet for 15 weeks beginning when mice were 8 weeks old. Adiposity measured by DEXA scan. **b,g**, Adipose-specific IDOL knockout mice ($n=13$ *Idol^{fl/fl}*, $n=17$ *Idol^{fl/fl}*/*Cre^{AdipoQ}*) fed a western diet for 15 weeks starting when the mice were 6 weeks old. Adiposity measured by MRI. **c,h**, Endothelium-specific IDOL knockout mice ($n=21$ *Idol^{fl/fl}*, $n=22$ *Idol^{fl/fl}*/*Cre^{Cdh5}*) fed a western diet for 15 weeks starting when the mice were 6 weeks old. Adiposity measured by MRI. **d,i**, Intestine-specific IDOL knockout mice ($n=13$ *Idol^{fl/fl}*, $n=19$ *Idol^{fl/fl}*/*Cre^{Vil}*) fed a western diet for 15 weeks starting when the mice were 6 weeks old. Adiposity measured by MRI. **e,j**, Muscle-specific IDOL knockout mice ($n=11$ *Idol^{fl/fl}*, $n=18$ *Idol^{fl/fl}*/*Cre^{Mck}*) fed a western diet for 15 weeks starting when the mice were 6 weeks old. Adiposity measured by MRI. There were no statistically significant differences between groups in any panel of this figure. The precise n , P values, and details of the statistical testing are listed in the source data file.

over-abundance of VLDLR protein (Extended Data Fig. 4a,b), has an even more pronounced protective effect on wild-type mice, but has no additional effect on the background of VLDLR deficiency. These data strongly suggest that altered abundance of VLDLR and not LDLR is an important contributor to systemic energy balance.

We assessed metabolic fitness in the compound mutant mice by performing a glucose tolerance test after 6 weeks on a HFHC diet (Fig. 3c) and an insulin tolerance test after 10 weeks on this diet (Fig. 3d). Both the IDOL knockout and IDOL-LDLR double-knockout groups had improved glucose clearance and enhanced response to a bolus of insulin relative to the wild-type group; however, the IDOL-VLDLR double-knockout group was indistinguishable from the wild-type group. These data were analysed by comparing the areas under the curves (AUCs) using a one-way analysis of variance (ANOVA) (Fig. 3g,h). Collectively, these data provide strong evidence for the idea that regulation of VLDLR protein levels is important for the maintenance of metabolic homoeostasis.

Acute knockdown of IDOL in the central nervous system increases energy expenditure. VLDLR is most highly expressed in the brain, muscle, fat, and endothelium. Having ruled out the peripheral metabolic tissues as the source of the IDOL–VLDLR effect on energy balance, we considered the CNS as a potential site of action. Previous studies showed that the IDOL pathway in the CNS affects the function of both microglia and neurons^{29,30}; however, the possibility that central actions of IDOL affect metabolism has not been addressed. To test whether IDOL was acting centrally, we developed a CNS-optimized antisense oligonucleotide (ASO) targeting *Idol*. Dose-response studies determined that 40 µg given by intracerebroventricular injection was the minimum dose required for maximal suppression of *Idol* expression in whole-brain homogenates collected 2 weeks after the injection (Extended Data Fig. 5a). Using this optimized protocol, we knocked down *Idol*

expression in 5-week-old C57Bl/6J mice and initiated a western diet-induced obesity study 1 week after injection. At the end of the 7-week western diet study, *Idol* expression was suppressed by 65% in the hypothalamus of ASO-injected mice relative to vehicle-treated control mice (Fig. 4a). As expected, *Idol* knockdown in the CNS was associated with increased VLDLR protein in the hypothalamus (Fig. 4c). The mice treated with the IDOL ASO weighed less than their control counterparts after 6 weeks on the western diet (Fig. 4b, $P < 0.01$ by repeat measures two-way ANOVA). These findings were confirmed in a second cohort of mice using a CNS-optimized negative control ASO (Extended Data Fig. 5b). Consistent with the whole-body knockout, the *Idol* ASO-treated mice were leaner by MRI analysis (Fig. 4d) and had smaller fat pads on dissection (Extended Data Fig. 5c,d).

Although IDOL ASO-treated mice mimicked the phenotype of the whole-body IDOL knockout mice, we did not observe changes in food intake. We postulated that the body weight difference may involve changes in energy expenditure. We performed indirect calorimetry on the cohorts after 2–3 weeks on the western diet (before their body mass and adiposity diverged, Extended Data Fig. 5e). The ASO-treated mice exhibited increased energy expenditure (Fig. 4f), determined with two different data analysis methods: the NIDDK Mouse Metabolic Phenotyping Centers energy expenditure analysis (<https://www.mmpc.org/shared/regression.aspx>), and the BWH-Harvard web application for indirect calorimetry analysis (<https://calrapp.org/>)³¹. The treatment effect was significant ($P < 0.05$ by analysis of covariance (ANCOVA)) when either the overall mean total body mass or the mean lean body mass of each treatment group was used as the covariate. The increased energy expenditure could not be explained by changes in locomotor activity (Fig. 4g,h).

The livers of the IDOL ASO-treated mice had less lipid deposition, similar to the global IDOL knockout mice (Extended Data Fig. 5f). The IDOL knockout mice also had smaller white adipose

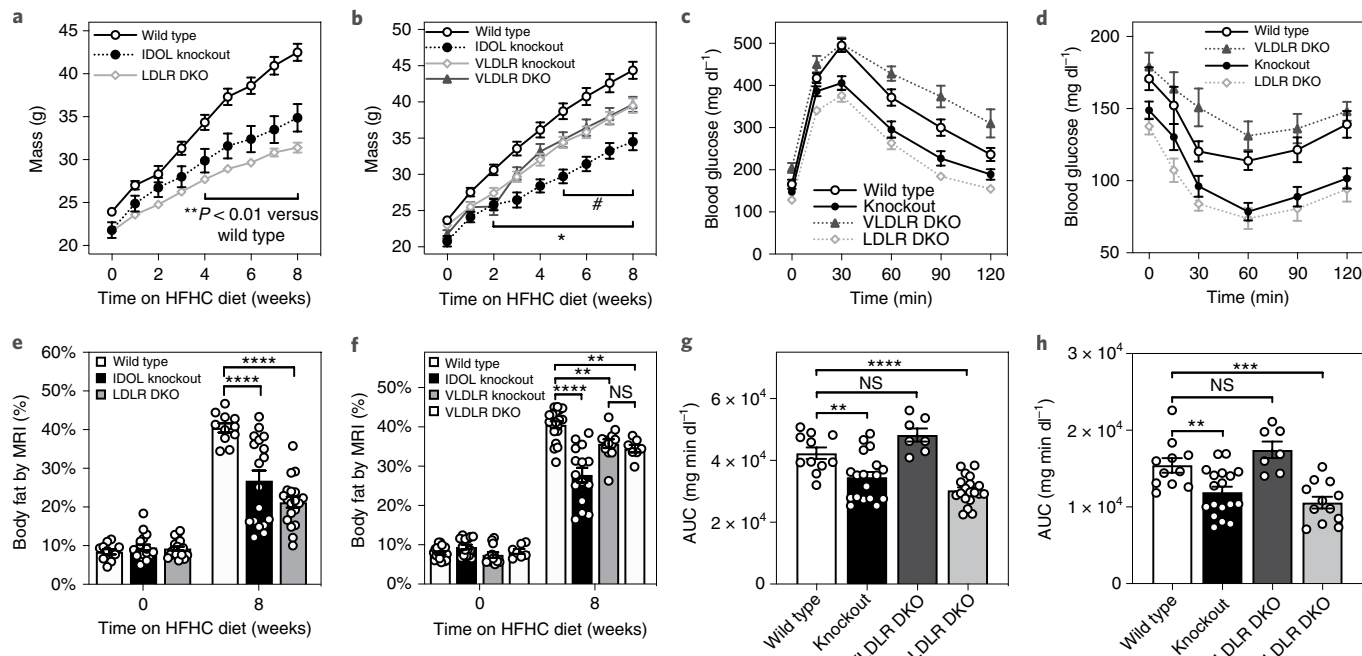


Fig. 3 | IDOL regulates systemic energy balance through VLDLR. **a**, Growth curves showing the mean mass \pm s.e.m. for male mice placed on a HFHC diet from 6–8 weeks of age. $n=11$ wild-type, $n=18$ *Idol*^{-/-} (knockout), $n=18$ *Idol*^{-/-}/*Ldlr*^{-/-} (LDLR double-knockout (DKO)) mice. **b**, Growth curves showing the mean mass \pm s.e.m. for male wild-type $n=20$, *Idol*^{-/-} (IDOL knockout) $n=15$, *Vldlr*^{-/-} (VLDLR knockout) $n=12$, and *Idol*/*Vldlr*^{-/-} (VLDLR DKO) $n=7$ mice fed an HFHC diet from 6–8 weeks of age. **c**, Intraperitoneal glucose tolerance test (1 g kg^{-1}) administered after 6 weeks on the HFHC diet. The values shown are the mean blood glucose levels \pm s.e.m. **d**, Intraperitoneal insulin tolerance test (1 U kg^{-1}) administered after 10 weeks on the HFHC diet. The values shown are the mean blood glucose levels \pm s.e.m. **e**, Adiposity reported as body fat percentage \pm s.e.m. measured by MRI for the mice reported in panel **a** at baseline and after 8 weeks on the HFHC diet. **f**, Adiposity reported as body fat percentage \pm s.e.m. measured by MRI for the mice reported in panel **c** at baseline and after 8 weeks on the HFHC diet. **g**, The AUC was calculated for the glucose tolerance test for each mouse and the mean values \pm s.e.m. and individual values are plotted. **h**, The AUC was calculated for the insulin tolerance test for each mouse and the mean values \pm s.e.m. and individual values are plotted. * $P<0.05$, ** $P<0.01$, *** $P<0.001$, **** $P<0.0001$. NS, not significant. The precise n , P values, and details of the statistical testing are provided in the source data file.

tissue depots containing smaller adipocytes, but we did not find an obvious increase in multi-locular cells resembling beige adipocytes (Fig. 4e). Histological analysis of brown adipose tissue revealed smaller cells with more abundant lipid droplets (Fig. 4e), consistent with increased energy expenditure. Increased brown adipose tissue activity is associated with alterations in glucose catabolism³², whereas acute pharmacological stimulation of brown adipose tissue can reduce circulating lipids by driving fatty acid oxidation³³. The ASO-treated mice appeared to have increased carbohydrate metabolism, but we did not observe a consistent change in fat oxidation (Extended Data Fig. 5g,h). ASO treatment increased the phosphorylation of hormone sensitive lipase (HSL) in the subcutaneous white adipose depot (Fig. 4i), a canonical downstream target of adrenergic receptor-mediated protein kinase A (PKA) stimulation³²; we also noted an increased abundance of tyrosine hydroxylase in the brown adipose tissue (Fig. 4j), consistent with increased catecholamine production by sympathetic nerves. These observations linked acute knockdown of *Idol* in the CNS to systemic changes in energy expenditure; however, they did not provide insight into the brain cell type (or types) responsible for the phenotype.

IDOL deletion alters hypothalamic gene expression linked to energy balance. The increased energy expenditure seen when CNS expression of *Idol* was knocked down suggests that IDOL regulates one or more energy homoeostasis circuits in the brain. We used Drop-seq, a single-cell RNA-sequencing technique, to obtain an overview of the changes in the transcriptional landscape of individual cell populations in the hypothalamus provoked by IDOL dele-

tion (Fig. 5a). We placed wild-type and IDOL knockout mice on a HFHC for 2 weeks and then analysed hypothalamic gene expression. Clustering algorithms successfully identified 26 populations of cells in the hypothalamus, including 11 non-neuronal populations and 15 distinct populations of neurons (Fig. 5b and Extended Data Fig. 6a–c). We analysed the dataset for *Vldlr* gene expression and found two clusters in which significant numbers of cells had high *Vldlr* expression: oligodendrocytes and neurons (Extended Data Fig. 6d). When the genotype of the neurons was unmasked, the clustering analysis revealed several populations of neurons that had incompletely overlapping clusters of wild-type and IDOL knockout cells (Fig. 5c). Such separations indicate altered global transcriptional profiles in these populations. We assessed two populations of cells that have been extensively studied for their contributions to energy homoeostasis: Agouti-related peptide (AGRP) neurons and pro-opiomelanocortin (POMC) neurons^{34,35}. A third population of cells, histaminergic neurons expressing *Slc18a2*, was also profiled because of its apparent reduction in the IDOL knockout mice; however, our analysis of transcriptional changes did not reveal any reason for the difference in this population. It is likely that the observed changes in cell abundance are an artefact of this cell population being a relatively under-represented cluster even in the wild-type mice.

Analysis of transcript abundance in the AGRP neurons revealed that loss of IDOL altered the expression of a range of genes linked to energy balance. Each of the labelled genes in each of the volcano plots in Figure 5d is annotated in genome-wide association studies (GWAS), OMIM, or PubMed as being associated with energy homoeostasis (Supplementary Table 2). The differentially expressed

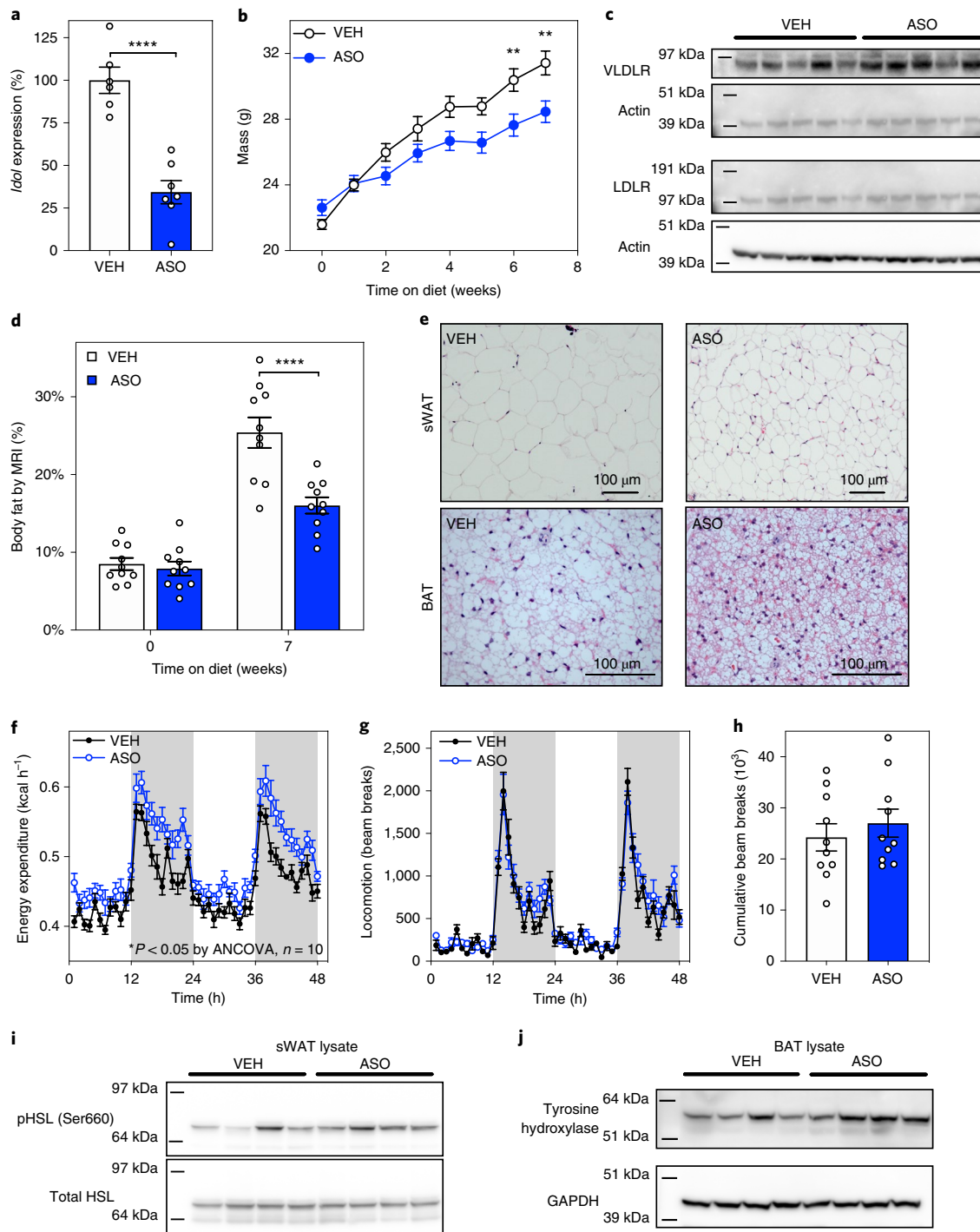


Fig. 4 | Acute knockdown of IDOL in the CNS reduces adiposity by increasing energy expenditure. **a**, Intracerebroventricular injection of a CNS-optimized ASO targeting *Idol* reduced *Idol* expression by 65% in the hypothalamus measured at study termination. The mean *Idol* expression \pm s.e.m. is shown. $P < 0.0001$ by two-tailed *t*-test, $n = 8$. **b**, Growth curve showing the mean mass \pm s.e.m. for male mice placed on western diet 1 week after injection of *Idol*-targeting ASO or vehicle control (VEH). ** $P < 0.01$ by repeat measures ANOVA, $n = 10$. **c**, Increased VLDLR protein levels in the hypothalamus of IDOL knockout mice 8 weeks after ASO injection. The blots are representative of two independent analyses. **d**, Adiposity reported as body fat percentage \pm s.e.m. measured by MRI. $n = 10$, **** $P < 0.0001$ by repeat measures ANOVA. **e**, Haematoxylin- and eosin-stained subcutaneous white adipose tissue (sWAT) and interscapular brown adipose tissue (BAT) sections from mice after 7 weeks of western diet feeding. A $\times 20$ objective lens was used for sWAT and a $\times 40$ objective lens was used for BAT. These images are representative of five independent biological replicates. **f**, Energy expenditure measured by indirect calorimetry in mice after 2–3 weeks on a western diet, showing the mean value per h \pm s.e.m. $n = 10$, * $P < 0.05$ VEH versus ASO by ANCOVA using either total body mass or lean body mass as covariates. **g**, Locomotor activity as measured when a mouse crossed multiple infrared beams during the calorimetry experiment. Mean values \pm s.e.m. are shown for ten mice. **h**, No difference was seen in the overall locomotion of mice as quantified by the cumulative number of beam breaks in a 48 h period \pm s.e.m. $P = 0.4772$ by two-tailed *t*-test, $n = 10$. **i**, Western blot analysis of the phosphorylation of HSL in sWAT. This blot is representative of two independent analyses. **j**, Western blot analysis of tyrosine hydroxylase abundance in the BAT. This blot is representative of two independent analyses. The precise n , P values, and details of the statistical testing are provided in the source data file.

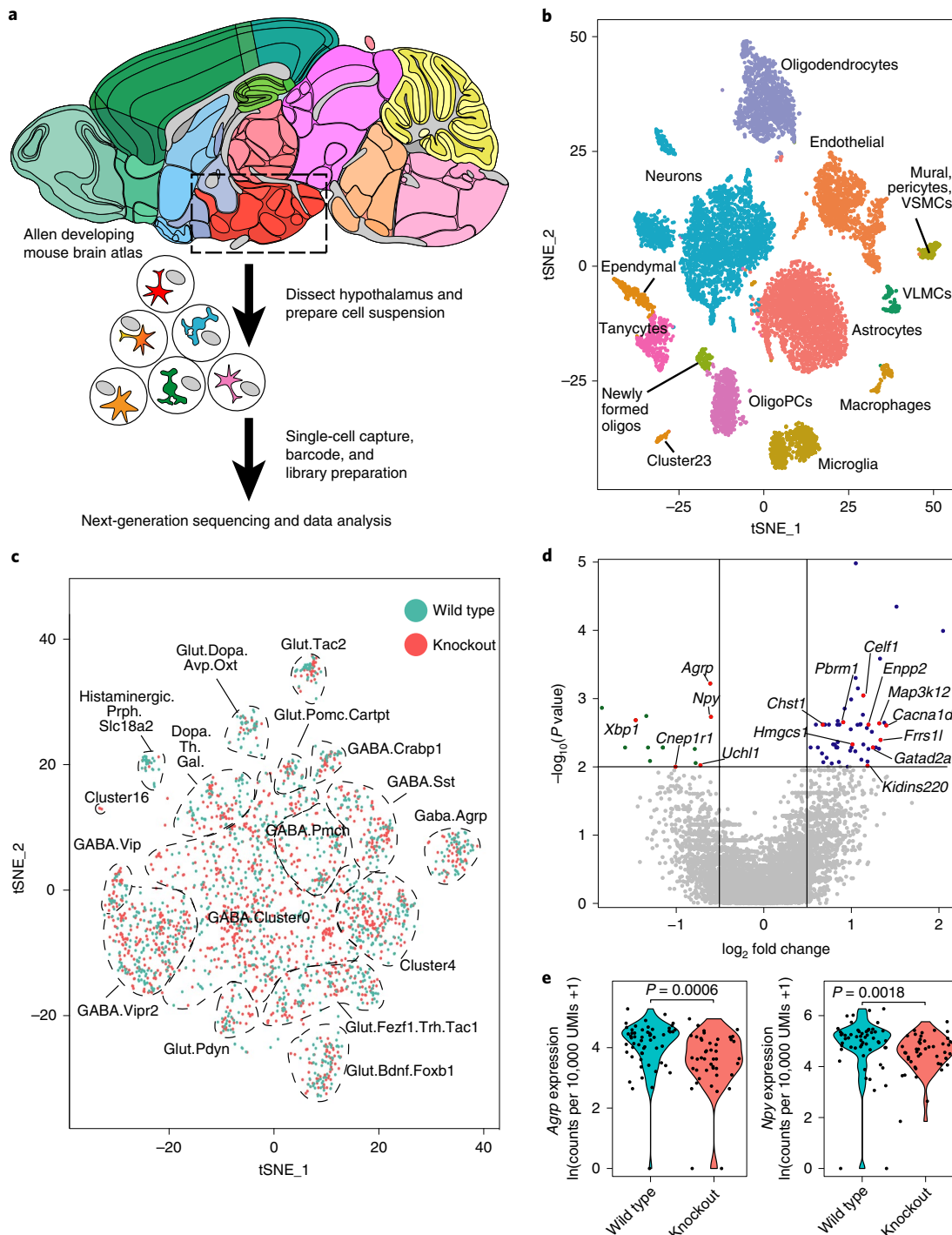


Fig. 5 | The single-cell transcriptional landscape of the hypothalamus is affected by deletion of IDOL. **a**, Simplified schematic of the single-cell RNA-seq experimental design. 5-week-old mice were placed on a HFHC diet for 2 weeks. Hypothalamic tissues from six mice ($n=3$ per group) were dissected and dissociated into single-cell suspension. Single cells and barcoded beads were captured into droplets, and this was followed by complementary DNA synthesis, amplification, and library preparation. The library was sequenced with an Illumina HiSeq 4000 next-generation instrument using the Drop-seq custom read 1B primer. **b**, Global gene expression relationships in the 11,453 single cells projected onto two dimensions using tSNE. The clusters were defined using shared nearest neighbour graph-based clustering. VSMCs, vascular smooth muscle cells; VLMCs, vascular and leptomeningeal cells; vascular smooth muscle cells (VSMCs); OligoPC, oligodendrocyte precursor cells. **c**, tSNE plot demonstrating the effect of IDOL knockout on the clustering of single cells in 15 different neuron clusters. $n=11,453$ cells. **d**, Volcano plot of the differentially expressed genes in AGRP neurons. Expression data calculated as counts per 10,000 unique molecular identities (UMIs). The P values were calculated using two-tailed Wilcoxon rank sum tests from $n=56$ wild-type and $n=45$ *Idol*^{-/-} neurons identified within the AGRP cluster. Labelled genes are linked to whole-body metabolic homeostasis (see Extended Data Table 1 for details). **e**, Violin plots demonstrating that IDOL deletion reduced gene expression of *Agrp* and *Npy* in AGRP neurons. Individual data points indicate the magnitude of gene expression in a single cell. These are superimposed on a probability density plot for the distribution of the data. Statistics were calculated using two-tailed Wilcoxon rank sum tests on non-Ln transformed data. $n=56$ wild-type and $n=45$ IDOL knockout neurons identified within the AGRP cluster.

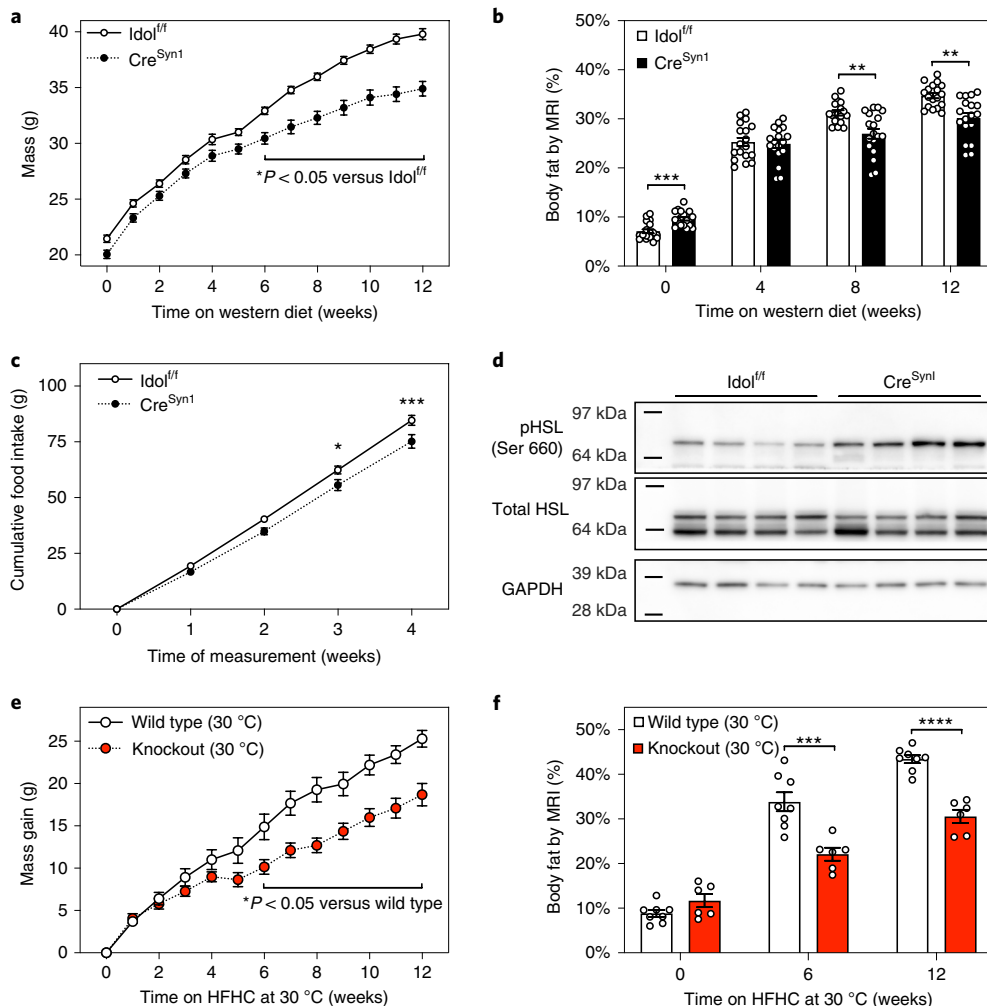


Fig. 6 | Conditional deletion of *Idol* from neurons drives the metabolic protection seen in global IDOL knockout mice. **a**, Growth curve showing the mean mass \pm s.e.m. **b**, Adiposity reported as body fat percentage \pm s.e.m., measured by MRI for three cohorts of neuron-specific IDOL conditional knockout mice fed a western diet starting at 5–6 weeks old. $n=18$ per genotype. * $P<0.05$, ** $P<0.01$, *** $P<0.001$ **** $P<0.0001$ *Idol^{fl/fl}* versus *Idol^{fl/fl}* *Cre^{Syn1}* mice by repeat measures ANOVA. **c**, Neuron-specific deletion of IDOL reduces food intake. The mean cumulative food consumption is shown \pm s.e.m. $n=7$ per genotype. * $P<0.05$, *** $P<0.001$ *Idol^{fl/fl}* versus *Idol^{fl/fl}* *Cre^{Syn1}* mice by repeat measures ANOVA. **d**, Increased phosphorylation of HSL in the subcutaneous white adipose tissue of neuron-specific conditional IDOL knockout mice. Each lane was loaded with a protein lysate from independent mice. This blot is representative of two independent repeats. **e,f**, Global IDOL knockout mice are protected from diet-induced mass gain and adiposity when group-housed at thermoneutrality. $n=6$ wild-type, $n=8$ IDOL knockout mice. **e**, Growth curve showing the mean mass gained \pm s.e.m. **f**, Adiposity reported as body fat percentage \pm s.e.m., measured by MRI. * $P<0.05$, ** $P<0.001$, *** $P<0.0001$ wild type versus knockout by repeat-measures ANOVA. The precise n , P values, and details of the statistical testing are provided in the source data file.

genes identified in AGRP neurons showed an enrichment of these genes (Fig. 5d). Modest differences were also observed between genotypes in POMC and histaminergic neurons (Extended Data Fig. 6e,f). Interestingly, two key orexigenic genes were downregulated in the AGRP neurons of IDOL knockout mice: the genes encoding AGRP and neuropeptide Y (Fig. 5e). AGRP neurons have also been associated with the negative regulation of energy expenditure^{36–38}. Collectively, these data reveal that deletion of IDOL in the CNS altered the transcriptional regulation of several key neural circuits known to regulate energy balance.

IDOL deletion in neurons regulates energy balance. We followed up on the ASO and single-cell RNA-sequencing results by creating pan-neuron conditional knockout mice by crossing the *Idol^{fl/fl}* mice with SynI-Cre transgenic mice (*Idol^{fl/fl}; Cre^{Syn1}*). Similar to the global knockout mice, the *Cre^{Syn1}Idol^{fl/fl}* mice had reduced mass and adiposity when challenged with the western diet (Fig. 6a,b, $n=18$). Again,

we conducted long-term food intake measurements to maximize our ability to detect small changes in food intake. As shown in Figure 6c, the *Cre^{Syn1}Idol^{fl/fl}* mice consumed less food per week than their *Idol^{fl/fl}* littermates. This finding shows that the changes in food intake in IDOL-deficient mice are the result of primary IDOL effects in neurons. We assessed energy expenditure by indirect calorimetry but did not detect any statistically significant differences between the two groups. Western blot analysis of subcutaneous white adipose tissue showed enhanced phosphorylation of HSL in *Cre^{Syn1}Idol^{fl/fl}* mice (Fig. 6d). The activation of HSL clearly indicates that deletion of IDOL from neurons affected peripheral energy homeostasis; however, if changes in whole-body energy expenditure were present they were too subtle for the calorimeter to detect.

To distinguish the relative contributions of reduced food intake and increased energy expenditure to the IDOL knockout phenotype, we endeavoured to minimize the energy expenditure effects by housing the mice at thermoneutrality (30 °C for 12 weeks). Relative

to wild-type mice, global IDOL knockout mice gained less mass and adiposity on the obesogenic HFHC diet, suggesting that changes in food intake were sufficient to affect body weight in the absence of differences in energy expenditure (Fig. 6e,f).

We endeavoured to identify a specific hypothalamic locus driving the IDOL knockout phenotype; however, viral-Cre-mediated deletion of IDOL in neurons in the arcuate nucleus, or the paraventricular nucleus of the hypothalamus was not sufficient to recapitulate the *Cre^{SynI}Idol^{fl/fl}* mouse phenotype (Extended Data Fig. 7). Although the results of our viral experiments did not allow us to identify a precise neuron population responsible for the IDOL knockout phenotype, our work with the SynI-Cre mice clearly demonstrated that deletion of IDOL from neurons protected mice against diet-induced obesity by reducing food intake while enhancing energy expenditure pathways. These results further identified IDOL-mediated regulation of neuronal VLDLR as a previously unrecognized modulator of whole-body energy homoeostasis.

Discussion

The ability of an organism to adapt to changing nutritional availability is fundamental to its survival. A multitude of mechanisms for maintaining whole-body energy homoeostasis have been selected for over the course of mammalian evolution. In this study, we identify the IDOL–VLDLR pathway in neurons as a previously unknown modulator of whole-body energy homoeostasis. Two independent lines of global IDOL knockout mice (one derived at UCLA and one at AstraZeneca) exhibited a highly reproducible phenotype of resistance to diet-induced obesity. Despite the abundant expression of IDOL and its targets in adipose tissue, tissue-specific studies suggested that the CNS is the primary site of IDOL action in the regulation of energy balance. Loss of VLDLR but not LDLR expression on an IDOL knockout background abolished the protective effects of IDOL deficiency on the development of obesity.

Previous studies have established the molecular mechanisms by which IDOL regulates the abundance of its lipoprotein receptor targets. IDOL forms a homodimer that recognizes a specific conserved amino acid sequence in its membrane-bound targets for recognition and ubiquitin transfer. So far only three proteins have been identified that meet this stringent criterion: LDLR and its two most closely related family members, VLDLR and ApoER2. Although unexpected, our finding that VLDLR expression is required for the effects of IDOL on whole-body metabolism is consistent with prior work demonstrating that VLDLR is important in metabolic homoeostasis. One of the initial observations made by Herz and colleagues when they developed the VLDLR knockout mice was that the mice exhibited a reduction in mass and body-mass index relative to wild-type controls on a mixed background²⁷. These findings were confirmed by other groups^{22,28} and we replicated this finding again here (Fig. 3). Previous mechanistic analyses have suggested that VLDLR in the periphery acts in the endothelium to enhance lipoprotein lipase-dependent hydrolysis of triglycerides^{20–23}. However, it is important to point out that the consequence of IDOL deficiency is increased, rather than decreased, VLDLR protein levels. Coupled with prior work, our results suggest that the appropriate balance of VLDLR protein levels in the CNS is important for the maintenance of whole-body energy homoeostasis.

While this article was under review, Van Loon et al.³⁹ described a similar phenotype of obesity resistance in the UCLA-generated IDOL knockout mouse line, which we had previously provided to them. These authors attributed the body weight differences in global IDOL knockout mice to IDOL activity in the liver, based on correlations between hepatic *Idol* expression and metabolic parameters in a C57BL/6J × DBA/2J (BXD) dataset. By contrast, our data do not support a causal role for hepatic IDOL in the phenotype. We tested the role of IDOL in the liver directly with hepatocyte-specific conditional IDOL knockout mice (Albumin-Cre, Fig. 2) and found that loss of liver IDOL did not confer protection against diet-

induced metabolic dysfunction. Furthermore, the only lipoprotein receptor target of IDOL that is expressed by the liver is LDLR, which we unequivocally demonstrated was not required for the effects of IDOL on the response to a HFD (Fig. 3a,b). Nevertheless, we conclude that the phenotype of the UCLA global IDOL knockout mice is consistent between different vivarium conditions.

Although energy balance is maintained by multiple brain regions^{40,41}, the role of the hypothalamus is particularly prominent^{34,42}. Acting via the sympathetic nervous system^{32,43,44}, the hypothalamus is a key effector of CNS influence on adipose tissue, including response to cold. It has also been implicated in the metabolic actions of leptin^{36,45}, FGF21 (ref. 46), PPAR γ agonists^{47,48}, and thyroid hormone^{49,50}. We observed increased VLDLR protein levels in the hypothalamus of both IDOL knockout mice and IDOL-ASO-treated mice, suggesting that this region probably contributes to the metabolic effects of IDOL. Furthermore, our single-cell RNA-seq analysis demonstrated that deletion of IDOL altered the transcriptional landscape in several populations of neurons with well-established roles in the regulation of energy balance.

We investigated the potential for IDOL to regulate central control of metabolism using a combination of acute and chronic interventions, each of which provided insight into the physiological role of IDOL. The acute nature of the ASO studies allowed us to detect increased energy expenditure at a whole-organism level, linking IDOL in the CNS to peripheral energy homoeostasis. We did not detect changes in food intake during a 2-week-long evaluation, perhaps due to differences between chronic deletion of IDOL and acute knockdown, or due to the duration of the food intake study.

Based on the *Vldlr* expression pattern seen in our single-cell RNA-seq data, we focused our attention on IDOL in neurons. The complete loss of IDOL from neurons provided evidence that IDOL regulates food intake, consistent with the reduced expression of *Agrp* and *Npy* seen in our single-cell RNA-seq data of whole-body IDOL knockout mice. The relative importance of altered food intake to the phenotype was confirmed by thermoneutrality studies showing that body weight differences persisted when the role of thermogenesis was minimized.

Unfortunately, we have not yet been able to identify specific hypothalamic regions involved in the effects of IDOL on energy balance. We acknowledge that the viral-Cre approach used here suffers from the inherent weakness that the SynI promoter-driven Cre will be expressed in all infected neurons, which might obscure the role of specific neuronal populations⁵¹. Individual populations of neurons within a given hypothalamic nucleus may have opposing effects, as with POMC and AGRP neurons in the arcuate nucleus⁵².

Collectively, our studies identify the IDOL–VLDLR pathway as a previously unrecognized mode of regulating whole-body energy homoeostasis. We expect that this observation will prompt further investigation into the specific cellular mechanism (or mechanisms) by which cell-surface VLDLR levels regulate energy balance. The CNS contains a specific set of lipoproteins. Both ApoE and ApoJ (also called clusterin), two apolipoproteins found in cerebrospinal fluid, are known ligands for VLDLR^{26,53,54}. Several non-apolipoprotein ligands have also been proposed for VLDLR, including reelin² and F-spondin⁵⁵. Although there is evidence that ApoJ can bind to leptin and modulate the leptin response in cell culture⁵⁶, so far none of these ligands has conclusively been shown to regulate whole-body energy homoeostasis. In the periphery, VLDLR has a clear role in facilitating the lipolytic activity of lipoprotein lipase^{20,22}, and thereby in enhancing the release of free fatty acids. Free fatty acid sensing by the hypothalamus is a well-established modulator of neuronal activity⁵⁷, affecting peripheral metabolism^{58–60}, but the role of central VLDLR in this process has not been explored. Future studies will be required to define precisely how IDOL activity in the brain conveys a VLDLR-dependent signal to the periphery to regulate energy balance and which specific neuronal populations are involved.

Methods

Contact for reagent and resource sharing. Further information and requests for resources and reagents should be directed to, and will be fulfilled by, the lead contact, Peter Tontonoz (PTontonoz@mednet.ucla.edu). The antisense oligonucleotides were provided by IONIS Pharmaceuticals and are subject to a material transfer agreement between Ionis Pharmaceuticals and UCLA.

Experimental models. The UCLA line of IDOL knockout mice was generated with a gene trap cassette inserted in intron 1, which could be released with FRT recombination to create conditional knockout mice in which exon 2 was ‘flossed’⁶¹. All UCLA mice were studied after ten backcrosses to C57Bl/6J mice.

The AstraZeneca line of IDOL knockout mice was bred to a pure C57Bl/6N strain such that exon 2 was flanked by loxP sites. Whole-body IDOL knockout mice were derived from this strain by crossing the *Idol*^{fl/fl} mice with Rosa26-Cre transgenic mice. This strain was also used to create hepatocyte-specific *Idol*^{fl/fl} mice by crossing with Albumin-Cre transgenic mice⁶².

The aP2-IDOL transgenic mice were generated at the UCLA core facility. We cloned a dominant active form of human *IDOL* (K293R, K309R, K310R, K320R) into a pBluescript vector containing the 5.4 kb Fabp4 enhancer–promoter (a gift from Ronald Kahn, Joslin Diabetes Center) followed by bovine growth hormone polyA. The linearized construct was gel purified and microinjected into C57Bl/6J mice fertilized zygotes. Founders were identified using the following PCR primers (forward, GCCAGGAGGGCTCTGTACA; reverse, GAATAGAACATGACACCTACTCAGACAAT).

The mouse studies conducted at UCLA were reviewed and approved by the Chancellor’s Animal Research Committee. The mouse studies conducted by AstraZeneca were approved by Gothenburg Ethics Committee for Experimental Animals, license number 38-2011.

Mouse studies. All studies were performed with male mice in climate-controlled facilities maintained on a 12 h light–dark cycle at a constant temperature of 22 °C with group-housed mice, unless otherwise noted. Pilot studies used both male and female mice; however, female mice are resistant to diet-induced obesity and required prolonged challenges with more severe diets to elicit changes in adiposity. Consequently, male mice were used for all subsequent studies. For LFD and HFHC studies with the AstraZeneca mouse lines, dietary challenge was initiated in 8-week-old littermate mice. Body weights were recorded on a weekly basis. Body length (nose to base of the tail) was assessed at 4 and 20 weeks of age. Food intake in AstraZeneca mice was measured at 15 weeks of age by fasting mice for 12 h during the dark period before single-housing them in cages (23 × 16 cm) with pre-weighed aliquots of food for 48 h. Body composition was assessed in 20-week-old mice by dual energy X-ray absorptiometry (DEXA, GE Lunar) in isoflurane-anaesthetized mice. Metabolic fitness was determined by oral glucose tolerance tests (2 g kg⁻¹) performed at 22 weeks of age. The energy content of the faeces was determined using a bomb calorimeter (C 5000, IKA Werke). For the preliminary western diet and HFD studies (Fig. 1 and Extended Data Fig. 1), we placed littermate mice aged 5–6 weeks old on test diets for 15 weeks and measured body mass weekly. We separated the mice to measure food intake at week 12 before returning them to group housing. Metabolic fitness was determined by administering an intraperitoneal glucose tolerance test (1 g kg⁻¹) at week 9, and an intraperitoneal insulin tolerance test (1 U kg⁻¹) at week 14. We measured body composition by MRI after 15 weeks on the western diet (EchoMRI, 3-in-1). For western diet-fed conditional knockout studies, we placed littermate mice aged 5–6 weeks old on the diet for 15 weeks and measured their body mass weekly. We measured adiposity by MRI at baseline, then every four weeks until study termination. Metabolic fitness was determined with an intraperitoneal glucose tolerance test (1 g kg⁻¹) at 6 weeks and an intraperitoneal insulin tolerance test (1 U kg⁻¹) at 10 weeks. For the HFHC diet-fed single- and double-knockout studies, we placed male mice aged 7–8 weeks old on the HFHC diet and measured mass, adiposity, and metabolic fitness as described for the western diet conditional knockout studies above. Each cohort in the double-knockout studies was arranged to maximize the number of littermate controls. Double-knockout mice had single-knockout littermate controls, whereas single knockouts had wild-type littermate controls. For the western diet ASO study, we performed a pilot dose–response study in 5-week-old male C57Bl/6J mice to determine the minimum dose of ASO given by intracerebroventricular injection required for the maximal suppression of *Idol* expression in whole-brain homogenates relative to vehicle control-treated mice (Extended Data Fig. 5A). For the adiposity studies, 5-week-old male C57Bl/6J mice ordered from The Jackson Laboratory were administered 40 µg ASO or 10 µL vehicle control by intracerebroventricular injection. The study was repeated using 40 µg IDOL-targeting ASO or 40 µg control ASO. The mice recovered for 1 week before we initiated the dietary challenge. We measured energy expenditure by indirect calorimetry after 2–3 weeks of western diet feeding (OxyMax CLAMS, Columbus Instruments). We measured adiposity by MRI at baseline, immediately before the calorimetry experiments, at 4 weeks on the diet, and at 7 weeks on the diet, just before study termination. Mice were singly housed from the time they were moved to the metabolic chambers until the end of the study. We monitored food intake from week 4 to week 7.

For the food intake studies, littermate mice were singly housed in standard housing and fed a western diet ad libitum. The mass of diet administered and consumed was recorded weekly.

For the thermoneutrality studies, littermate mice were group housed in monitored climate-controlled facilities maintained on a 12 h light–dark cycle at a constant temperature of 30 °C.

For the virogenetic studies 10-week-old littermate UCLA-derived *Idol*^{fl/fl} male mice were anaesthetized with isoflurane and received analgesics (0.01 mg ml⁻¹ buprenorphine and 0.58 mg ml⁻¹ carprofen) before and after surgery. The AAV-hSyn-GFP or AAV-hSyn-GFP-Cre (UNC Vector Core, titre $\geq 6 \times 10^{12}$ vg ml⁻¹) was injected bilaterally into the following brain regions with the listed coordinates and volumes: arcuate nucleus, anterior–posterior (A–P) –1.57 mm from bregma, lateral ± 0.2 mm from bregma, dorsal–ventral (D–V) 5.8 mm from the cortex, 125 nl per side; paraventricular nucleus of the hypothalamus, A–P –0.33 mm from bregma, lateral ± 0.25 mm from bregma, D–V 4.4 mm from the cortex, 250 nl per side; ventromedial hypothalamus, A–P –1.6 mm from bregma, lateral ± 0.45 mm from bregma, D–V 5.4 mm from the cortex, 200 nl per side. Mice were allowed to recover for 1 week before starting on a western diet for 1 week; energy expenditure was then measured using the OxyMax CLAMS system. Following completion of the energy expenditure study, the mice were singly housed and food intake was measured as described above. At study termination (all cohorts), mice were fasted for 6 h beginning at 8:00 am, then euthanized by isoflurane overdose, and exsanguinated by cardiac puncture before cervical dislocation. Blood was collected in EDTA-coated tubes and centrifuged at 2000 g for 15 min to separate plasma. Tissues were collected from the mice and either snap-frozen in liquid nitrogen or fixed in 4% paraformaldehyde.

ASO production. ASOs targeting IDOL (5'-TTCCTTTTCCACACGCCA-3') were provided by Ionis Pharmaceuticals. Complete ASO chemistry information is as follows. IDOL ASO (Tes Tes mCes mCeO Tes Tds Tds Tds Tds Tds mCds mCds Ads mCds Ads mCeO Ges mCes mCes Ae) and control ASO (mCes mCeO Teo AeO Tes Ads Gds Gds Ads mCds Tds Ads Tds mCds mCds Aeo Geo Geo Aes Ae), where capital letters indicate base abbreviation: m, 5-methylcytosine; e, 2'-O-methoxyethylribose (MOE); k, (S)-2',4'-constrained 2'-O-ethyl (cEt); d, deoxyribose; s, phosphorothioate; and o, phosphodiester^{63–65}.

Gene expression. Differences in gene expression were determined by real-time quantitative PCR with reverse transcription (RT–qPCR) (Diagenode) from RNA isolated from frozen tissues with TRIzol (Life Technologies) according the manufacturer’s instructions.

Western blot analysis. Proteins were isolated from frozen tissue using a Dounce homogenizer on ice with RIPA buffer (Boston Bioproducts) containing phosphatase and protease inhibitors (Roche). Equal masses of proteins were separated by electrophoresis through Bis-Tris gels before being transferred to PVDF membrane. The membranes were probed using the antibodies listed in the key resources table.

Histology. Tissues were fixed in 4% paraformaldehyde and stored in ethanol before being mounted in paraffin. Sections (10 µm) were cut and stained with haematoxylin and eosin by the UCLA Translational Pathology Core.

Single-cell RNA-seq. Single-cell preparation. Single-cell suspensions were generated at a final concentration of 100 cells per µl in 0.01% BSA (in PBS) by digesting freshly dissected hypothalamus tissue with papain (Worthington Biochemical). Briefly, the hypothalamus was rapidly dissected then transferred into 4 ml ice-cold HABG (Hibernate A (HA, BrainBits), B27 (Invitrogen), and Glutamax (Thermo Fisher Scientific)) and incubated in a water bath at 30 °C for 8 min^{66,67}. The supernatant was discarded, and the remaining tissue was incubated with papain (12 mg in 6 ml Hibernate A with no calcium) at 30 °C for 30 min. After incubation, the papain solution was removed from the tissue and the tissue was washed with HABG three times. Using a siliconized 9 inch Pasteur pipette with a fire-polished tip, the suspension was triturated approximately ten times in 45 s. Next, the cell suspension was carefully applied to the top of the prepared OptiPrep density gradient (Sigma-Aldrich). The gradient was then centrifuged at 800 g for 15 min at 22 °C. We aspirated the top 6 ml containing cellular debris. To dilute the gradient material, we mixed the desired cell fractions with 5 ml HABG. The cell suspension containing the desired cell fractions was centrifuged for 3 min at 22 °C at 200 g, and the supernatant containing the debris was discarded. Finally, the cell pellet was loosened by flicking the tube and the cells were resuspended in 1 ml 0.01% BSA (in PBS). This final cell suspension solution was passed through a 40 µm strainer (Thermo Fisher Scientific) to discard debris, followed by cell counting.

Drop-seq single-cell barcoding, library preparation, and sequencing. Drop-seq was performed using standard methodology⁶⁸, with the following modifications: the number of beads in a single PCR tube was increased to 4,000 per tube, the number of PCR cycles was increased to 4 + 11 cycles, and multiple PCR tubes were pooled before size selection and purification with AMPure XP (Beckman Coulter). The libraries were then checked on a TapeStation (Agilent) for library quality, average size, and estimation of the concentration. The samples were then tagmented using the Nextera DNA Library Preparation kit (Illumina) and multiplex indices

were added. The Drop-seq library molar concentration was quantified by Qubit Fluorometric Quantitation (Thermo Fisher Scientific) and library fragment length was estimated using a TapeStation. Sequencing was performed on an Illumina HiSeq 4000 instrument (Illumina) using the Drop-seq custom read 1B primer (Integrated DNA Technologies). 100 bp paired end reads were generated with an 8-bp index read for multiplexing. Read 1 consists of the 12 bp cell barcode, followed by the 8 bp unique molecular identity. Read 2 contains the single-cell transcripts.

Drop-seq data pre-processing and quality control. The demultiplexed fastq files from the Drop-seq sequencing data were processed into a digital gene expression matrix using the dropSeqPipe (<https://github.com/Hoohm/dropSeqPipe>) SnakeMake wrapper for Drop-seq tools version 1.13. Briefly, read pairs with a quality score of less than 10 were discarded, then transcript reads were trimmed to remove template-switching-oligonucleotide contamination and polyA tails and aligned to mm10 using STAR v2.5.0c with default settings. A digital gene expression matrix for each sample was generated in which each row is the read count of a gene and each column a unique single cell. The transcript counts of each cell were normalized by the total number of unique molecular identities for that cell. These values were then multiplied by 10,000 and Ln transformed. Digital gene expression matrices from the six samples (three wild-type and three knockout samples) were combined to create a pooled digital gene expression matrix. Single cells were identified from background noise using a threshold of at least 250 genes and 500 transcripts, resulting in a dataset of 6,600 cells from IDOL knockout samples and 4,800 cells from wild-type samples.

Identification of cell clusters. The Seurat R package (version 2.3.1, <https://github.com/satijalab/seurat>) was used to project all sequenced cells onto two dimensions using t-distributed stochastic neighbour embedding (tSNE) and shared nearest neighbour graph-based clustering⁶⁹ was used to define clusters. To further refine the neuronal cell clusters, clusters expressing neuronal-specific markers were pooled and re-analysed separately in a similar manner, considering only this neuronal subset. Briefly, the most highly variable genes were identified using the mean and dispersion (variance/mean), which were used to scale and centre the data. Principal components analysis was performed on this normalized data and significant principal components were identified using the JackStraw permutation-based approach⁷⁰. These significant principal components were used in tSNE to project the data onto two dimensions and graph-based clustering was used to identify cell clusters.

Resolving cell identities of the cell clusters. To resolve the identities of the cell clusters, known cell type-specific markers from previous studies were curated and checked for expression patterns within the cell clusters. A cluster showing high expression levels of a known marker gene specific for a particular cell type was considered to carry the identity of that cell type. Known markers for major hypothalamus cell types and neuronal subtypes were retrieved from Romanov⁷¹, Chen et al.⁷², and Campbell et al.⁷³. These markers were sufficient to define all major cell types as well as neuronal subpopulations.

Identification of differentially expressed genes between the wild type and knockout. Within each identified cell type, single cells from wild-type and knockout samples were compared for differential gene expression using a Wilcoxon rank sum test. To be considered in the analysis, the gene had to be expressed in at least 25% of the single cells from one of the two groups within that cell type and there had to be at least a 0.25 log fold change in gene expression between the groups.

Data quantification and statistical analysis. All data except the energy expenditure data were analysed using GraphPad Prism v7 with a predetermined α value of 0.05. The values reported in the text and figures are the group means \pm s.e.m. where n refers to the number of animals per group. The data were analysed for the assumptions of parametric statistical methods (equal variance and normal distribution) and log-transformed if required. If the log-transformed data did not meet the assumptions of parametric statistical methods, the non-transformed data were analysed using a non-parametric method, including the Mann–Whitney U test and the Wilcoxon rank sum test, as indicated in the appropriate figure legend. Parametric comparisons between two groups were done by t -tests and comparisons of multiple groups with a single independent factor were done by one-way ANOVA. If a parameter was measured over time, then data were analysed by repeat measures two-way ANOVA with time as one independent factor. The glucose- and insulin-tolerance tests were analysed by calculating the AUC for each mouse and then analysing the AUC data set by t -test or one-way ANOVA, as appropriate.

The energy expenditure data generated by the indirect calorimetry experiment were analysed using two methods: the NIDDK Mouse Metabolic Phenotyping Centers method, using their energy expenditure analysis page (<http://www.mmpc.org/shared/regression.aspx>); and the R programming language with CalR, a custom package for analysis of indirect calorimetry using analysis of covariance with a graphical user interface (<https://calr.bwh.harvard.edu>)³¹.

Reporting Summary. Further information on research design is available in the Nature Research Reporting Summary linked to this article.

Data Availability

The data that support the findings of this study are available from the corresponding author upon request and the Reporting Summary is available from the Nature Metabolism website. The single-cell RNA-seq data has been deposited in the NCBI Gene Expression Omnibus, accession number [GSE119960](#). Source data for Figs. 1–6 and Extended Data Figs. 1 and 3–7 are available online.

Received: 15 June 2018; Accepted: 12 September 2019;

Published online: 28 October 2019

References

- Goldstein, J. L. & Brown, M. S. A century of cholesterol and coronaries: from plaques to genes to statins. *Cell* **161**, 161–172 (2015).
- Trommsdorff, M. et al. Reeler/disabled-like disruption of neuronal migration in knockout mice lacking the VLDL receptor and ApoE receptor 2. *Cell* **97**, 689–701 (1999).
- Goldstein, J. L., DeBose-Boyd, R. A. & Brown, M. S. Protein sensors for membrane sterols. *Cell* **124**, 35–46 (2006).
- Lee, S. D. & Tontonoz, P. Liver X receptors at the intersection of lipid metabolism and atherosclerosis. *Atherosclerosis* **242**, 29–36 (2015).
- Hong, C. & Tontonoz, P. Liver X receptors in lipid metabolism: opportunities for drug discovery. *Nat. Rev. Drug. Discov.* **13**, 433–444 (2014).
- Rayner, K. J. et al. MiR-33 contributes to the regulation of cholesterol homeostasis. *Science* **328**, 1570–1573 (2010).
- Sallam, T. et al. Feedback modulation of cholesterol metabolism by the lipid-responsive non-coding RNA LeXis. *Nature* **534**, 124–128 (2016).
- Zelcer, N., Hong, C., Boyadjian, R. & Tontonoz, P. LXR regulates cholesterol uptake through Idol-dependent ubiquitination of the LDL receptor. *Science* **325**, 100–104 (2009).
- Hong, C. et al. The E3 ubiquitin ligase IDOL induces the degradation of the low density lipoprotein receptor family members VLDLR and ApoER2. *J. Biol. Chem.* **285**, 19720–19726 (2010).
- Scotti, E. et al. IDOL stimulates clathrin-independent endocytosis and multivesicular body-mediated lysosomal degradation of the low-density lipoprotein receptor. *Mol. Cell. Biol.* **33**, 1503–1514 (2013).
- Zhang, L., Xu, M., Scotti, E., Chen, Z. J. & Tontonoz, P. Both K63 and K48 ubiquitin linkages signal lysosomal degradation of the LDL receptor. *J. Lipid Res.* **54**, 1410–1420 (2013).
- Zhang, L. et al. The IDOL-UBE2D complex mediates sterol-dependent degradation of the LDL receptor. *Genes Dev.* **25**, 1262–1274 (2011).
- Calkin, A. C. et al. FERM-dependent E3 ligase recognition is a conserved mechanism for targeted degradation of lipoprotein receptors. *Proc. Natl Acad. Sci. USA* **108**, 20107–20112 (2011).
- Hong, C. et al. The LXR-Idol axis differentially regulates plasma LDL levels in primates and mice. *Cell Metab.* **20**, 910–918 (2014).
- Teslovich, T. M. et al. Biological, clinical and population relevance of 95 loci for blood lipids. *Nature* **466**, 707–713 (2010).
- Sorrentino, V. et al. Identification of a loss-of-function inducible degrader of the low-density lipoprotein receptor variant in individuals with low circulating low-density lipoprotein. *Eur. Heart J.* **34**, 1292–1297 (2013).
- Weissglas-Volkov, D. et al. The N342S MYLIP polymorphism is associated with high total cholesterol and increased LDL receptor degradation in humans. *J. Clin. Invest.* **121**, 3062–3071 (2011).
- Calkin, A. C. et al. Transgenic expression of dominant-active IDOL in liver causes diet-induced hypercholesterolemia and atherosclerosis in mice. *Circ. Res.* **115**, 442–449 (2014).
- Eguchi, J. et al. Transcriptional control of adipose lipid handling by IRF4. *Cell Metab.* **13**, 249–259 (2011).
- Yagyu, H. et al. Very low density lipoprotein (VLDL) receptor-deficient mice have reduced lipoprotein lipase activity. Possible causes of hypertriglyceridemia and reduced body mass with VLDL receptor deficiency. *J. Biol. Chem.* **277**, 10037–10043 (2002).
- Garcia-Arcos, I. et al. Adipose-specific lipoprotein lipase deficiency more profoundly affects brown than white fat biology. *J. Biol. Chem.* **288**, 14046–14058 (2013).
- Goudriaan, J. R. et al. The VLDL receptor plays a major role in chylomicron metabolism by enhancing LPL-mediated triglyceride hydrolysis. *J. Lipid Res.* **45**, 1475–1481 (2004).
- Obunike, J. C. et al. Transcytosis of lipoprotein lipase across cultured endothelial cells requires both heparan sulfate proteoglycans and the very low density lipoprotein receptor. *J. Biol. Chem.* **276**, 8934–8941 (2001).
- Alva, J. A. et al. VE-Cadherin-Cre-recombinase transgenic mouse: a tool for lineage analysis and gene deletion in endothelial cells. *Dev. Dyn.* **235**, 759–767 (2006).
- Bruning, J. C. et al. A muscle-specific insulin receptor knockout exhibits features of the metabolic syndrome of NIDDM without altering glucose tolerance. *Mol. Cell* **2**, 559–569 (1998).
- Andersen, O. M. et al. Essential role of the apolipoprotein E receptor-2 in sperm development. *J. Biol. Chem.* **278**, 23989–23995 (2003).

27. Frykman, P. K., Brown, M. S., Yamamoto, T., Goldstein, J. L. & Herz, J. Normal plasma lipoproteins and fertility in gene-targeted mice homozygous for a disruption in the gene encoding very low density lipoprotein receptor. *Proc. Natl. Acad. Sci. USA* **92**, 8453–8457 (1995).
28. Goudriaan, J. R. et al. Protection from obesity in mice lacking the VLDL receptor. *Arterioscler. Thromb. Vasc. Biol.* **21**, 1488–1493 (2001).
29. Choi, J. et al. The E3 ubiquitin ligase Idol controls brain LDL receptor expression, ApoE clearance, and A β amyloidosis. *Sci. Transl. Med.* **7**, 314ra184 (2015).
30. Gao, J. et al. The E3 ubiquitin ligase IDOL regulates synaptic ApoER2 levels and is important for plasticity and learning. *eLife* **6**, 1741 (2017).
31. Mina, A. I. et al. CalR: a web-based analysis tool for indirect calorimetry experiments. *Cell Metab.* **28**, 656–666 (2018).
32. Cannon, B. & Nedergaard, J. Brown adipose tissue: function and physiological significance. *Physiol. Rev.* **84**, 277–359 (2004).
33. Berbée, J. F. P. et al. Brown fat activation reduces hypercholesterolaemia and protects from atherosclerosis development. *Nat. Commun.* **6**, 6356 (2015).
34. Gautron, L., Elmquist, J. K. & Williams, K. W. Neural control of energy balance: translating circuits to therapies. *Cell* **161**, 133–145 (2015).
35. Tschöp, M. H. et al. A guide to analysis of mouse energy metabolism. *Nat. Methods* **9**, 57–63 (2012).
36. Caron, A., Lee, S., Elmquist, J. K. & Gautron, L. Leptin and brain-adipose crosstalks. *Nat. Rev. Neurosci.* **19**, 153–165 (2018).
37. Kong, D. et al. GABAergic RIP-Cre neurons in the arcuate nucleus selectively regulate energy expenditure. *Cell* **151**, 645–657 (2012).
38. Ruan, H.-B. et al. O-GlcNAc transferase enables AgRP neurons to suppress browning of white fat. *Cell* **159**, 306–317 (2014).
39. van Loon, N. M. et al. Inactivation of the E3 ubiquitin ligase IDOL attenuates diet-induced obesity and metabolic dysfunction in mice. *Arterioscler. Thromb. Vasc. Biol.* **38**, 1785–1795 (2018).
40. Waterson, M. J. & Horvath, T. L. Neuronal regulation of energy homeostasis: beyond the hypothalamus and feeding. *Cell Metab.* **22**, 962–970 (2015).
41. Nectow, A. R. et al. Identification of a brainstem circuit controlling feeding. *Cell* **170**, 429–442.e11 (2017).
42. Williams, K. W. & Elmquist, J. K. From neuroanatomy to behavior: central integration of peripheral signals regulating feeding behavior. *Nat. Neurosci.* **15**, 1350–1355 (2012).
43. Chechi, K., Carpenter, A. C. & Richard, D. Understanding the brown adipocyte as a contributor to energy homeostasis. *Trends Endocrinol. Metab.* **24**, 408–420 (2013).
44. Bamshad, M., Song, C. K. & Bartness, T. J. CNS origins of the sympathetic nervous system outflow to brown adipose tissue. *Am. J. Physiol.* **276**, R1569–R1578 (1999).
45. Friedman, J. 20 years of leptin: leptin at 20: an overview. *J. Endocrinol.* **223**, T1–T8 (2014).
46. Owen, B. M. et al. FGF21 acts centrally to induce sympathetic nerve activity, energy expenditure, and weight loss. *Cell Metab.* **20**, 670–677 (2014).
47. Lu, M. et al. Brain PPAR- γ promotes obesity and is required for the insulin-sensitizing effect of thiazolidinediones. *Nat. Med.* **17**, 618–622 (2011).
48. Xu, Y., O’Malley, B. W. & Elmquist, J. K. Brain nuclear receptors and body weight regulation. *J. Clin. Invest.* **127**, 1172–1180 (2017).
49. López, M. et al. Hypothalamic AMPK and fatty acid metabolism mediate thyroid regulation of energy balance. *Nat. Med.* **16**, 1001–1008 (2010).
50. Alvarez-Crespo, M. et al. Essential role of UCP1 modulating the central effects of thyroid hormones on energy balance. *Mol. Metab.* **5**, 271–282 (2016).
51. Mancini, G. & Horvath, T. L. Viral vectors for studying brain mechanisms that control energy homeostasis. *Cell Metab.* **27**, 1168–1175 (2018).
52. Schwartz, M. W., Woods, S. C., Porte, D., Seeley, R. J. & Baskin, D. G. Central nervous system control of food intake. *Nature* **404**, 661–671 (2000).
53. Leeb, C., Eresheim, C. & Nimpf, J. Clusterin is a ligand for apolipoprotein E receptor 2 (ApoER2) and very low density lipoprotein receptor (VLDLR) and signals via the Reelin-signaling pathway. *J. Biol. Chem.* **289**, 4161–4172 (2014).
54. Pohlkamp, T., Wasser, C. R. & Herz, J. Functional roles of the interaction of APP and lipoprotein receptors. *Front Mol. Neurosci.* **10**, 54 (2017).
55. Zisman, S. et al. Proteolysis and membrane capture of F-spondin generates combinatorial guidance cues from a single molecule. *J. Cell Biol.* **178**, 1237–1249 (2007).
56. Bajari, T. M., Strasser, V., Nimpf, J. & Schneider, W. J. A model for modulation of leptin activity by association with clusterin. *FASEB J.* **17**, 1505–1507 (2003).
57. Oomura, Y., Nakamura, T., Sugimori, M. & Yamada, Y. Effect of free fatty acid on the rat lateral hypothalamic neurons. *Physiol. Behav.* **14**, 483–486 (1975).
58. Lam, T. K. T. et al. Hypothalamic sensing of circulating fatty acids is required for glucose homeostasis. *Nat. Med.* **11**, 320–327 (2005).
59. Lam, T. K. T., Schwartz, G. J. & Rossetti, L. Hypothalamic sensing of fatty acids. *Nat. Neurosci.* **8**, 579–584 (2005).
60. Yue, J. T. Y. et al. A fatty acid-dependent hypothalamic-DVC neurocircuitry that regulates hepatic secretion of triglyceride-rich lipoproteins. *Nat. Commun.* **6**, 5970 (2015).
61. Scotti, E. et al. Targeted disruption of the idol gene alters cellular regulation of the low-density lipoprotein receptor by sterols and liver x receptor agonists. *Mol. Cell. Biol.* **31**, 1885–1893 (2011).
62. Postic, C. et al. Dual roles for glucokinase in glucose homeostasis as determined by liver and pancreatic beta cell-specific gene knock-outs using Cre recombinase. *J. Biol. Chem.* **274**, 305–315 (1999).
63. Swayze, E. E. et al. Antisense oligonucleotides containing locked nucleic acid improve potency but cause significant hepatotoxicity in animals. *Nucleic Acids Res.* **35**, 687–700 (2007).
64. Seth, P. P. et al. Synthesis and biophysical evaluation of 2',4'-constrained 2'O-methoxyethyl and 2',4'-constrained 2'O-ethyl nucleic acid analogues. *J. Org. Chem.* **75**, 1569–1581 (2010).
65. Østergaard, M. E. et al. Rational design of antisense oligonucleotides targeting single nucleotide polymorphisms for potent and allele selective suppression of mutant Huntington in the CNS. *Nucleic Acids Res.* **41**, 9634–9650 (2013).
66. Brewer, G. J. & Torricelli, J. R. Isolation and culture of adult neurons and neurospheres. *Nat. Protoc.* **2**, 1490–1498 (2007).
67. Poon, K., Barson, J. R., Fagan, S. E. & Leibowitz, S. F. Developmental changes in embryonic hypothalamic neurons during prenatal fat exposure. *Am. J. Physiol. Endocrinol. Metab.* **303**, E432–E441 (2012).
68. Macosko, E. Z. et al. Highly parallel genome-wide expression profiling of individual cells using nanoliter droplets. *Cell* **161**, 1202–1214 (2015).
69. Waltman, L. & van Eck, N. J. A smart local moving algorithm for large-scale modularity-based community detection. *Eur. Phys. J. B* **86**, 75 (2013).
70. Chung, N. C. & Storey, J. D. Statistical significance of variables driving systematic variation in high-dimensional data. *Bioinformatics* **31**, 545–554 (2015).
71. Romanov, R. A. et al. Molecular interrogation of hypothalamic organization reveals distinct dopamine neuronal subtypes. *Nat. Neurosci.* **20**, 176–188 (2017).
72. Chen, R., Wu, X., Jiang, L. & Zhang, Y. Single-cell RNA-seq reveals hypothalamic cell diversity. *Cell Rep.* **18**, 3227–3241 (2017).
73. Campbell, J. N. et al. A molecular census of arcuate hypothalamus and median eminence cell types. *Nat. Neurosci.* **20**, 484–496 (2017).

Acknowledgements

Further information and requests for resources and reagents should be directed to, and will be fulfilled by, the lead contact, Peter Tontonoz (P.Tontonoz@mednet.ucla.edu). Funding for this project was provided by grants to P.T. from the National Institutes of Health (HL066088, HL136618, and DK063491). S.D.L. was supported by a fellowship from the Canadian Institutes of Health Research and by a grant from the National Institutes of Health (P30 DK063491). C.P. was supported by an F32 fellowship from the National Institutes of Health (HL123236). A.C.C. was supported by a fellowship from the National Heart Foundation of Australia (O 08 M 3934). J.G. was supported by a K99/R00 pathway to independence award from the National Institutes of Health (AG054736). C.H. was supported by AHA grant 3BGIA17110079 and ADA grant 1-14-JF-33.

Author Contributions

S.D.L., C.P., S.M.C., X.Y., M.B., P. \ddot{A} ., D.L., H.B., and M.B.-Y. were responsible for conceptualization of the study. S.D.L., C.P., D.V.A., M.B., and P.T. were responsible for formal analysis. Funding was acquired by P.T. and by AstraZeneca AB. S.D.L., C.P., M.B., J.G., J.E.V., M.G.M., J.K., D.V.A., I.S.A., G.D., H.A., M.P., A.C., A.A., F.S., I.M., P.E., M.A., and C.H. were responsible for investigations. S.D.L., C.P., C.H., J.G., D.A., I.S.A., G.D., J.E.V., P.R., M.B., A.C.C., H.A., P. \ddot{A} ., D.L., H.B., M.B.-Y., S.M.C., X.Y., and P.T. were responsible for the methodology. M.B., M.A., P. \ddot{A} ., D.L., H.B., and P.T. were responsible for project administration. A.C.C., P.R., T.A.C., R.L., M.A., P. \ddot{A} ., H.B., M.B.-Y., S.M.C., X.Y., and P.T. were responsible for resources. P.T., X.Y., S.M.C., P. \ddot{A} ., D.L., H.B., and M.B.-Y. supervised the study. S.D.L., C.P., C.H., J.G., D.A., I.S.A., G.D., J.E.V., P.R., M.B., and A.C.C. were responsible for validation. S.D.L., C.P., M.B., D.V.A., J.E.V., S.M.C., and P.T. were responsible for visualization. S.D.L., P.T., and M.B. wrote the original draft. S.D.L., C.P., M.B., J.E.V., P. \ddot{A} ., D.L., H.B., M.B.-Y., S.M.C., and P.T. reviewed and edited the manuscript.

Competing interests

M.B., H.A., M.P., A.C., A.A., F.S., I.M., P.E., M.A., P. \ddot{A} ., D.L., H.B., and M.B.-Y. are employees of AstraZeneca AB. T.A.C. and R.L. are employees of Ionis Pharmaceuticals. The other authors have no competing interests.

Additional information

Extended data is available for this paper at <https://doi.org/10.1038/s42255-019-0127-7>.

Supplementary information is available for this paper at <https://doi.org/10.1038/s42255-019-0127-7>.

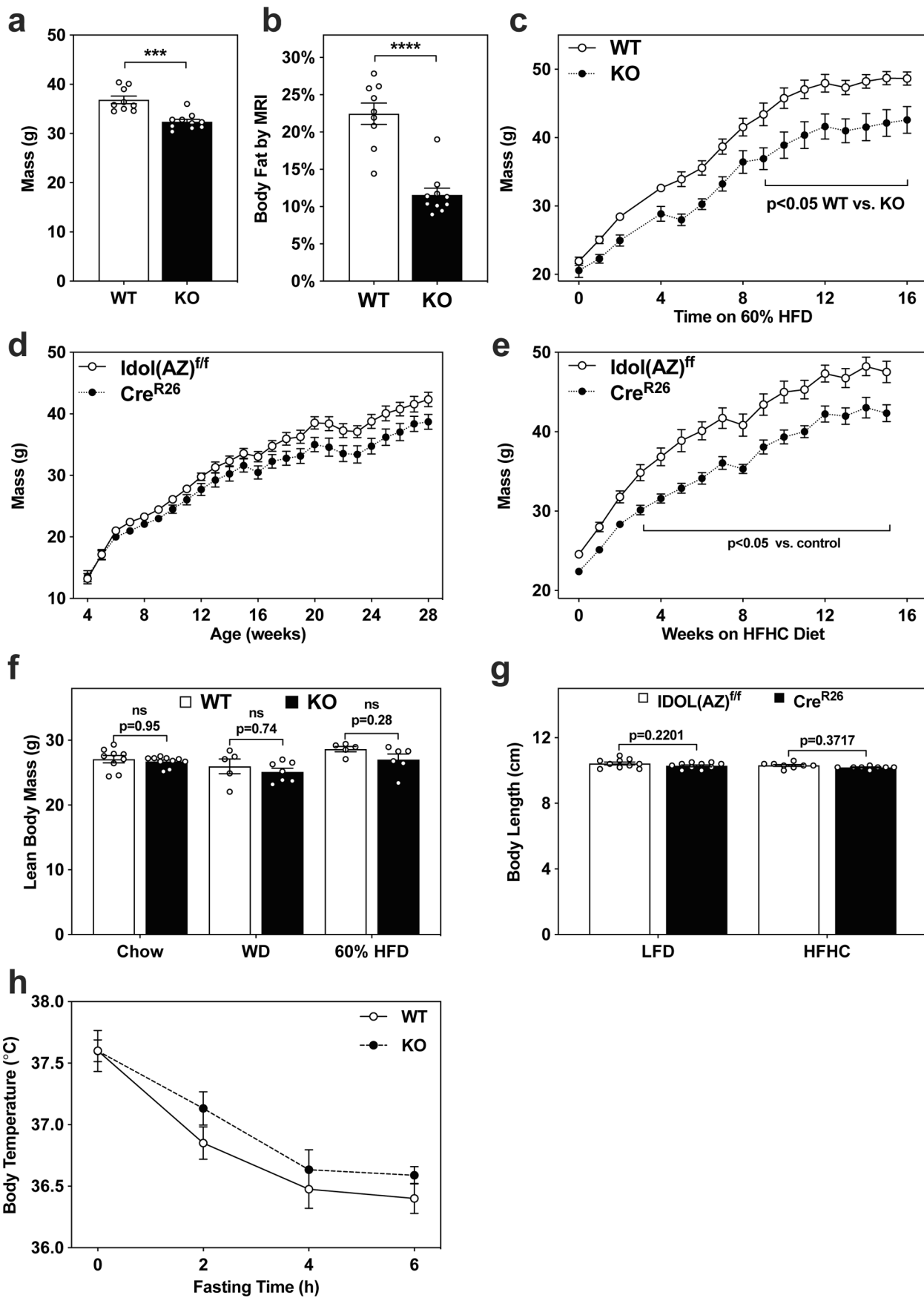
Correspondence and requests for materials should be addressed to P.T.

Peer review information Primary Handling Editor: Pooja Jha.

Reprints and permissions information is available at www.nature.com/reprints.

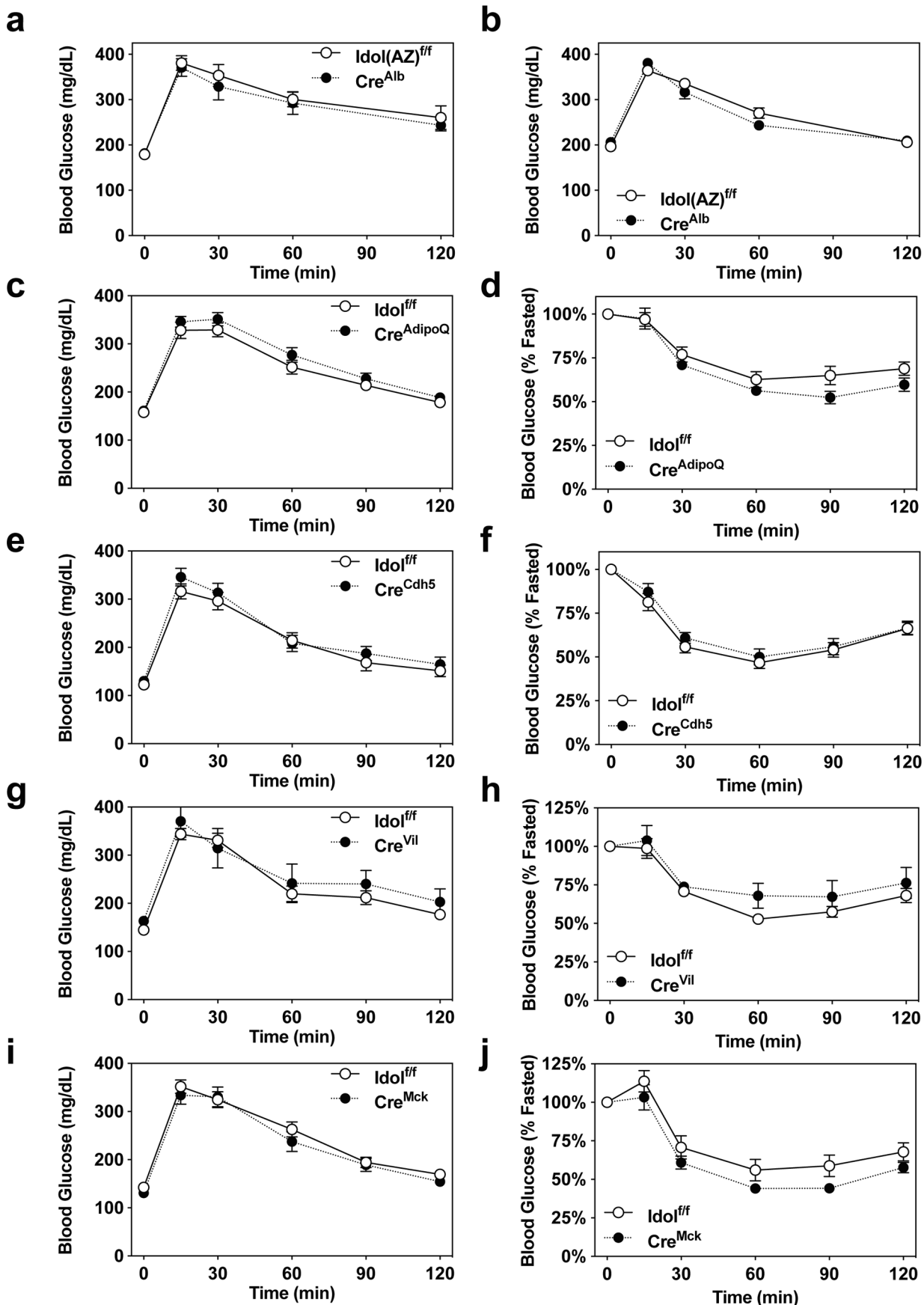
Publisher’s note Springer Nature remains neutral with regard to jurisdictional claims in published maps and institutional affiliations.

© The Author(s), under exclusive licence to Springer Nature Limited 2019



Extended Data Fig. 1 | See next page for caption.

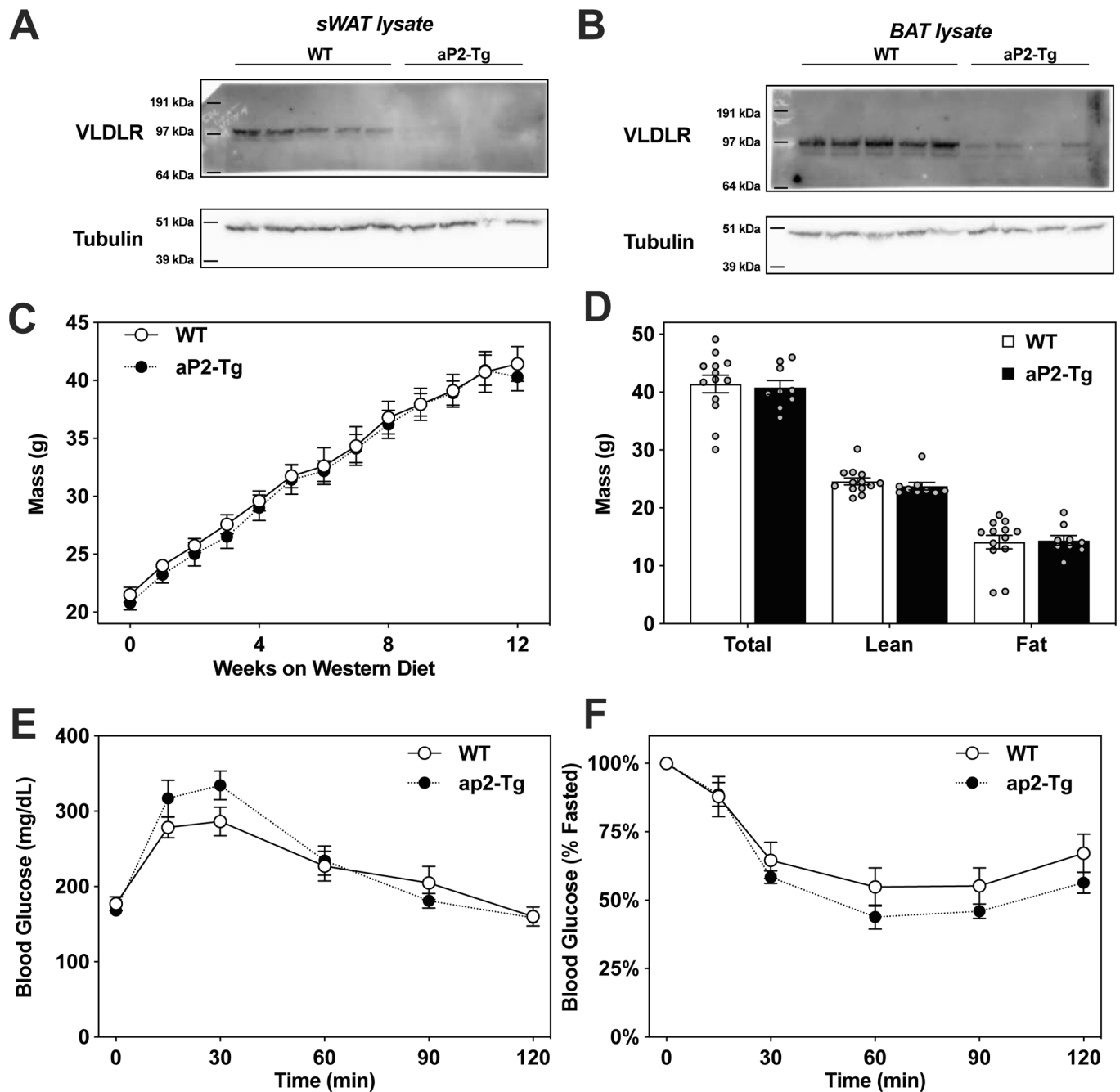
Extended Data Fig. 1 | Metabolic phenotype of IDOL-deficient mice. **a,b**, 18-month-old IDOL KO mice are protected against age-induced adiposity. **a**, Mean mass and standard error of the mean; n=9 WT, n=10 KO mice, ***p<0.001, ****p<0.0001 vs. WT by two-tailed t-test. **b**, Mean body fat percentage +/– the standard error of the mean; n=9 WT, n=10 KO mice, ***p<0.001, ****p<0.0001 vs. WT 2-tailed t-test. **c**, Growth curve for littermate male mice fed a 60% kcal high fat diet (HFD) starting when the mice were 6 weeks old. The mean values are shown +/– the standard error of the mean; n=5 WT and n=6 KO mice *p<0.05 by repeat measures ANOVA. **d**, Growth curve for littermate male IDOL(AZ)^{yf} mice with or without whole-body Rosa26 Cre fed a low-fat diet from 8 weeks of age. The mean mass is shown +/– SEM; n=10 mice per group. **e**, Growth curve for littermate male IDOL(AZ)^{yf} mice with or without whole-body Rosa26 Cre fed a high fat high cholesterol diet from 8-weeks of age; n=8 *Idol*(AZ)^{yf} mice n=9 *Cre*^{R26+}/*Idol*(AZ)^{yf} mice; *p < 0.05 by repeat measures ANOVA **f**, Unchanged lean body mass in male IDOL knockout mice administered test diets despite adiposity changes measured by MRI. Mean lean mass is shown +/– SEM; n=9 WT and n=10 KO mice fed Chow, n=5 WT and n=7 mice fed western diet, n=5 WT and n=6 KO mice fed the 60% HFD, p-values calculated by two-way ANOVA with Sidak post hoc tests. **g**, Body length measured from nose to anus at 20 weeks of age for male mice fed either a low-fat diet (LFD) or a high-fat high-cholesterol diet (HFHC) for 12 weeks. The mean values are shown +/– the standard error of the mean. Low-fat diet: n=10 mice per genotype. High Fat High Cholesterol diet: n=8 *Idol*(AZ)^{yf} mice and n=9 *Cre*^{R26+}/*Idol*(AZ)^{yf} mice. P-values calculated by repeat measures ANOVA. **h**, Mean body temperature +/– SEM measured rectally in response to fasting in mice fed a high-fat high-cholesterol diet; n=8 WT and n=9 IDOL KO mice. The precise n-number, p-value, and details of all statistical testing are provided in the source data file.



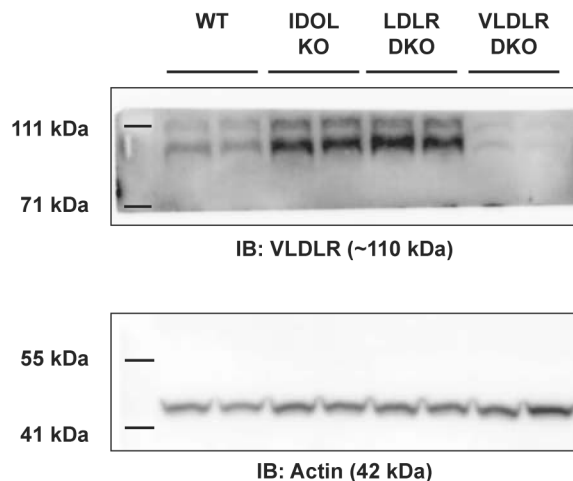
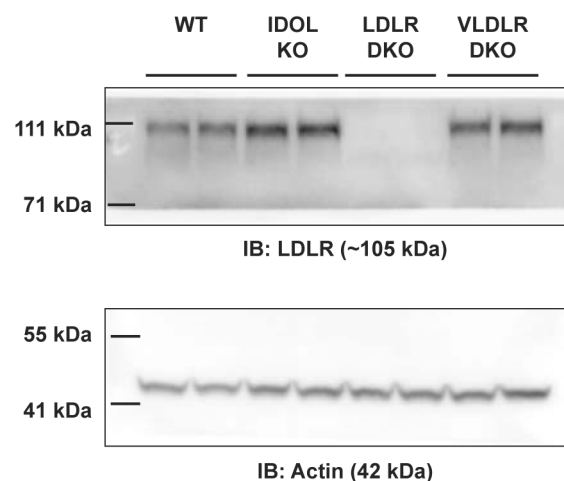
Extended Data Fig. 2 | See next page for caption.

Extended Data Fig. 2 | Glucose and insulin tolerance tests conducted on *Idol^{fl/fl}* and conditional knockouts with tissue-specific deletion of IDOL. a–b.

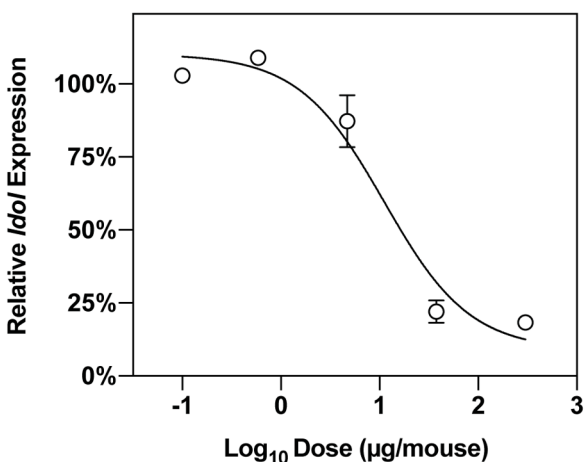
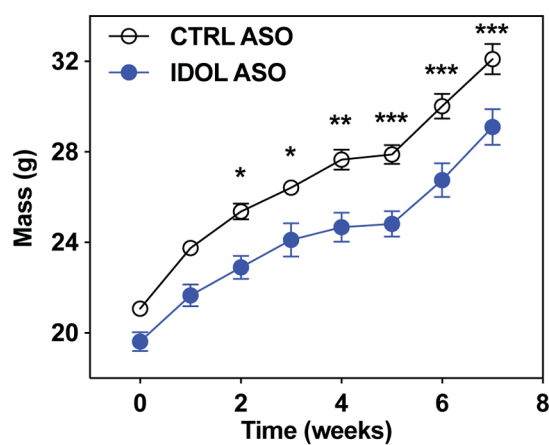
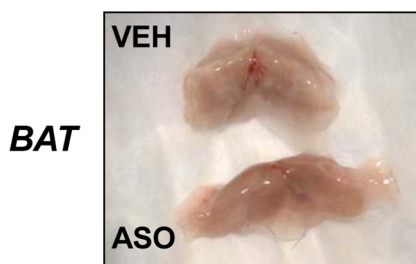
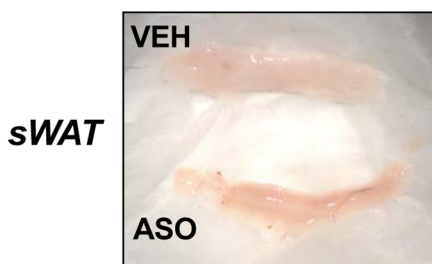
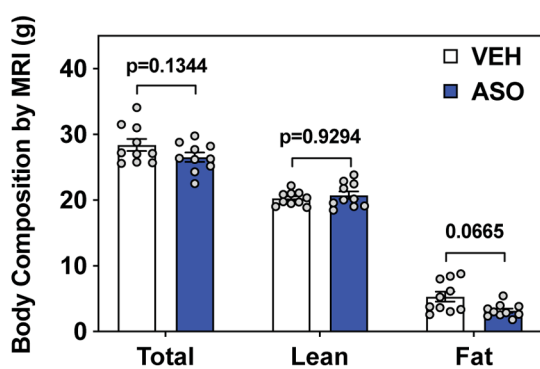
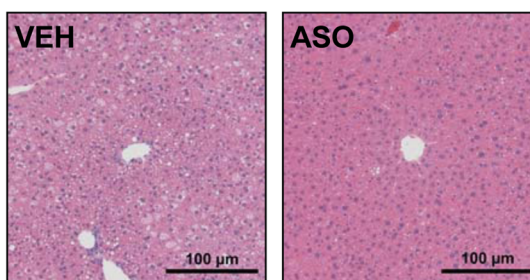
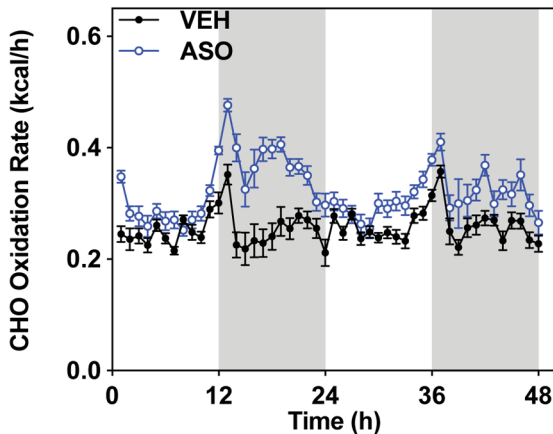
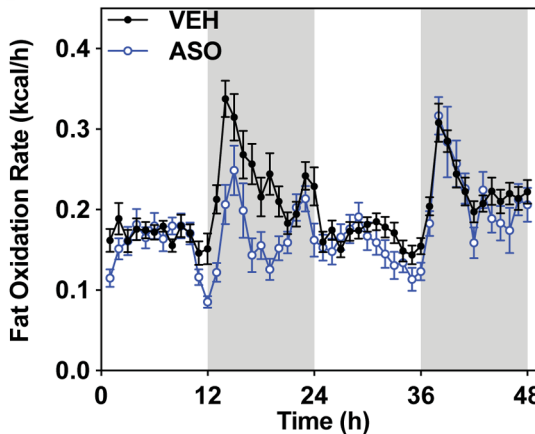
Mean blood glucose levels \pm SEM for liver-specific conditional IDOL KO mice challenged with an oral glucose tolerance test (2 g/kg) at 22 weeks of age fed either **a**, the low-fat diet; n=12 mice per genotype or **b**, the high-fat high-cholesterol diet for 16 weeks; n=11 mice per genotype. **c–j**, Mean blood glucose levels \pm SEM for male mice fed a western diet challenged with an intraperitoneal glucose tolerance test (1 g/kg, shown on the left) after six weeks on diet and an intraperitoneal insulin tolerance test (1 U/kg, shown on the right) after ten weeks on diet. **c,d**, Adipose-specific conditional IDOL KO; n=11 *Idol^{fl/fl}*, n=9 *Cre^{AdipoQ}Idol^{fl/fl}* mice. **e,f**, Endothelium-specific conditional IDOL KO; n=13 *Idol^{fl/fl}*, n=10 *Cre^{Cdhs}Idol^{fl/fl}* mice. **g,h**, Intestine-specific conditional IDOL KO; n=8 *Idol^{fl/fl}*, n=4 *Cre^{Vil}Idol^{fl/fl}* mice. **i,j**, Muscle-specific conditional IDOL KO; n=10 mice per genotype for the GTT and n=10 *Idol^{fl/fl}*, n=9 *Cre^{Mck}Idol^{fl/fl}* mice for the ITT.



Extended Data Fig. 3 | Adipose-specific transgenic *IDOL* mice are not protected from diet-induced obesity. **a**, Ablation of VLDLR protein levels in the subcutaneous inguinal white adipose tissue of the aP2-*IDOL* transgenic mice. This blot is representative of many independent experiments conducted by two independent researchers. **b**, Reduced VLDLR protein in the interscapular brown adipose tissue of the aP2-*IDOL* transgenic mice. This blot is representative of many independent experiments conducted by two independent researchers. **c**, Growth curve for WT and aP2-*IDOL* transgenic mice fed a western diet from 5 weeks of age showing the mean mass \pm SEM; $n=13$ WT and $n=9$ aP2-*IDOL* transgenic mice after 12 weeks of western diet feeding. **d**, Mean body composition measured by MRI \pm SEM for $n=13$ WT and $n=9$ aP2-*IDOL* transgenic mice after 12 weeks of western diet feeding. **e**, Intraperitoneal glucose tolerance test (1g/kg) administered after six weeks of western diet feeding; $n=13$ WT and $n=9$ aP2-*IDOL* transgenic mice. **f**, Intraperitoneal insulin tolerance test (1U/kg) administered after ten weeks of western diet feeding $n=13$ WT and $n=9$ aP2-*IDOL* transgenic mice.

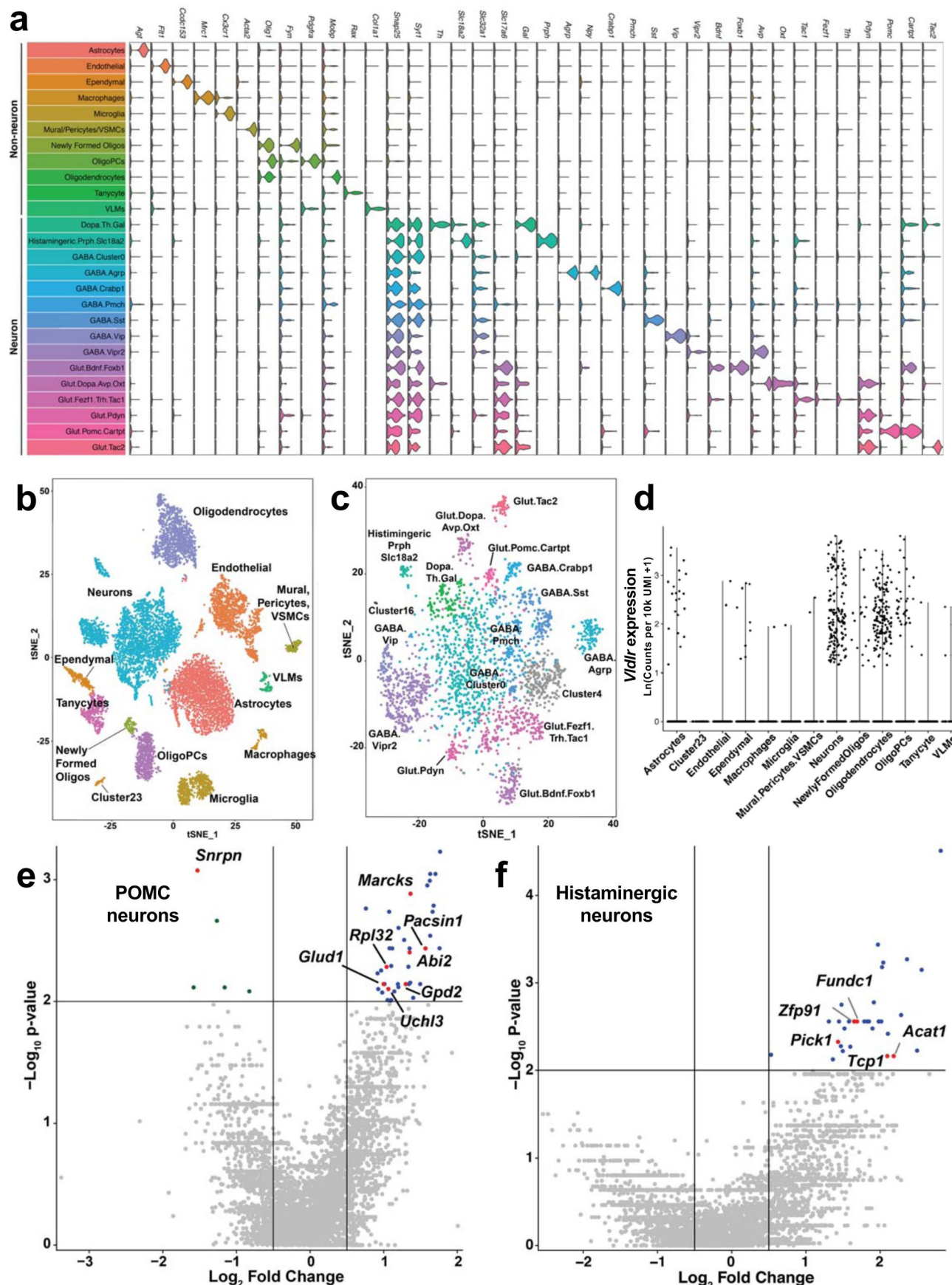
a**b**

Extended Data Fig. 4 | IDOL regulates systemic energy balance through the VLDL receptor. 100ug of RIPA isolate from the hypothalamus of individual wild-type (WT), *Idol*^{-/-} (KO), *Idol*^{-/-}*Ldlr*^{-/-} (LDLR DKO), or *Idol*^{-/-}*Vldlr*^{-/-} (VLDLR DKO) mice was loaded per lane of a Tris-Acetate NuPAGE gel. The image is representative of many independent experiments. These samples were repeated twice to assess reproducibility. **a**, Western blot analysis of VLDLR protein levels in the hypothalamus at study termination. **b**, Western blot analysis of LDLR protein levels in the hypothalamus at study termination.

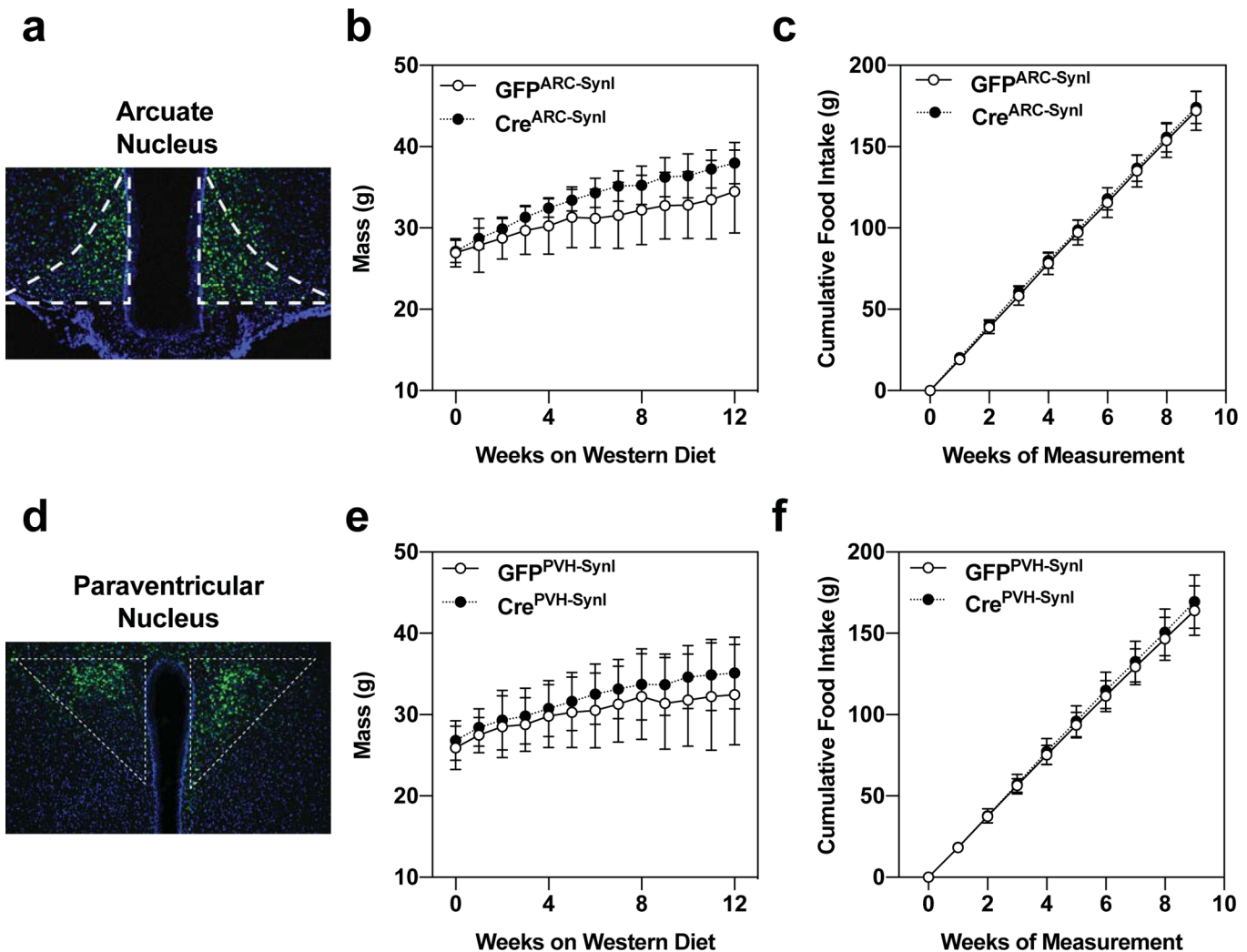
a**b****c****d****e****f****g****h**

Extended Data Fig. 5 | See next page for caption.

Extended Data Fig. 5 | Acute knockdown of *Idol* in the central nervous system increases energy expenditure. **a**, Optimization of the dose of ASO required to suppress *Idol* expression in whole-brain homogenates measured 8-weeks post-injection. The values represent the mean expression of *Idol* in a whole brain homogenate 8-weeks post-injection $+/-$ SEM; $n=4$ mice per time point. **b**, Growth curve for male mice placed on western diet one week after intracerebroventricular injection of *Idol*-targeting antisense oligonucleotide (IDOL ASO) or CNS-optimized control (CTRL ASO). The mean masses are shown $+/-$ SEM; $*p < 0.05$, $**p < 0.01$, $***p < 0.001$ by repeat measures two-way ANOVA, $n=10$ mice treated with CTRL and $n=5$ mice treated with IDOL ASO. **c**, Macroscopic view of interscapular brown adipose tissue depots after seven weeks on western diet. These images are representative of the ten mice per group in the ASO study. **d**, Macroscopic view of subcutaneous (inguinal) white adipose tissue depots after seven weeks on western diet. These samples are representative of the ten mice per group in the ASO study. **e**, No statistically significant differences in body composition at the onset of CLAMS experiment. The mean total body mass, lean body mass, and fat body mass are shown $+/-$ SEM; statistical significance determined by two-way ANOVA to account for multiple testing, $n=10$ mice per group. The precise n-number, p-value, and details of all statistical testing are provided in the source data file file. **f**, Reduced lipid accumulation in the livers of ASO treated mice evident with hematoxylin and eosin staining of $5\mu m$ sections of liver (10x objective). These images are representative of three mice per treatment group that were analysed for histology. **g**, Calculation of carbohydrate metabolism in the $n=10$ mice per group. The mean energy expenditure derived from carbohydrate metabolism for the mice in Fig. 4f is shown $+/-$ s.e.m. for each time point. **h**, Calculation of lipid oxidation in the $n=10$ mice per group. The mean energy expenditure derived from lipid metabolism for the mice in Fig. 4f is shown $+/-$ s.e.m. for each time point.



Extended Data Fig. 6 | Single cell RNA sequencing examination of the transcriptional landscape of the hypothalamus with Drop-seq. Clustering analysis combined with expression profiling of a panel of marker genes allowed us to discriminate 26 unique clusters of cells in the hypothalamus. **a**, Violin plots demonstrate the expression patterns of the 38 marker genes used to identify the cell clusters. Individual data points indicating the magnitude of gene expression in a single cell are superimposed on a probability density plot for the distribution of the data; the expression analysis is based on the data collected from $n=11,453$ single cells. **b**, Global gene expression relationships in the 11,453 single cells isolated from the hypothalamic tissues of six mice projected onto two dimensions using t-distributed Stochastic Neighbour Embedding (tSNE). The clusters were defined using shared nearest neighbour graph-based clustering. **c**, tSNE plot of the neuronal cells identified in the Drop-seq experiment ($n=3369$ single cells). **d**, Violin plot demonstrating that *Vldr* is only appreciably expressed in neuron and oligodendrocyte cell populations. Individual data points indicating the magnitude of gene expression in a single cell; the expression analysis is based on the unique molecular identities (UMI) data collected from $n=11,453$ single cells. **e-f**, Volcano plots of the differentially expressed genes analyzed by two-sided Wilcoxon rank sum tests in **e**, POMC⁺ ($n=24$ WT and $n=26$ *Idol*^{-/-} cells) and **f**, Histaminergic neurons ($n=23$ WT and $n=11$ *Idol*^{-/-} neurons. Labelled genes are linked to whole body metabolic homeostasis – see Supplemental Data Table 2 for details.



Extended Data Fig. 7 | Neuron-specific virogenetic deletion of IDOL from individual hypothalamic nuclei is insufficient to protect against diet-induced obesity. **a-c**, Adeno-associated virus (AAV) expressing either GFP-Cre or GFP regulated by the Synapsin I (Synl) promoter were injected into the arcuate nucleus (ARC; panels a-c) or the paraventricular nucleus of the hypothalamus (PVH; panels d-f). **a-c**, Deletion of IDOL from neurons in the ARC had no effect on body mass or food intake for mice fed a western diet for 12 weeks; n = 8 mice injected with AAV-expressing GFP (GFP^{ARC-Synl}), n = 8 mice injected with AAV expressing Cre-GFP (Cre^{ARC-Synl}). **a**, An image of the ARC showing GFP-positive cells to demonstrate successful infection of neurons; the image is representative of the sixteen mice injected in the ARC study. **b**, Growth curve showing the mean mass of the mice from each treatment group +/– one standard deviation. **c**, The mean cumulative mass of food consumed per mouse +/– one standard deviation. **d-f**, Deletion of IDOL from neurons in the PVH had no effect on body mass or food intake for mice fed a western diet for 12 weeks; n = 8 mice injected with AAV expressing GFP (GFP^{PVH-Synl}), n = 9 mice injected with AAV expressing Cre-GFP (Cre^{PVH-Synl}). **d**, An image of the PVH showing GFP-positive cells to demonstrate successful infection of neurons; the image is representative of the seventeen mice injected in the PVH experiment. **e**, Growth curve showing the mean mass of the mice from each treatment group +/– one standard deviation. **f**, The mean cumulative mass of food consumed per mouse +/– one standard deviation.

Reporting Summary

Nature Research wishes to improve the reproducibility of the work that we publish. This form provides structure for consistency and transparency in reporting. For further information on Nature Research policies, see [Authors & Referees](#) and the [Editorial Policy Checklist](#).

Statistics

For all statistical analyses, confirm that the following items are present in the figure legend, table legend, main text, or Methods section.

n/a Confirmed

- The exact sample size (n) for each experimental group/condition, given as a discrete number and unit of measurement
- A statement on whether measurements were taken from distinct samples or whether the same sample was measured repeatedly
- The statistical test(s) used AND whether they are one- or two-sided
Only common tests should be described solely by name; describe more complex techniques in the Methods section.
- A description of all covariates tested
- A description of any assumptions or corrections, such as tests of normality and adjustment for multiple comparisons
- A full description of the statistical parameters including central tendency (e.g. means) or other basic estimates (e.g. regression coefficient) AND variation (e.g. standard deviation) or associated estimates of uncertainty (e.g. confidence intervals)
- For null hypothesis testing, the test statistic (e.g. F , t , r) with confidence intervals, effect sizes, degrees of freedom and P value noted
Give P values as exact values whenever suitable.
- For Bayesian analysis, information on the choice of priors and Markov chain Monte Carlo settings
- For hierarchical and complex designs, identification of the appropriate level for tests and full reporting of outcomes
- Estimates of effect sizes (e.g. Cohen's d , Pearson's r), indicating how they were calculated

Our web collection on [statistics for biologists](#) contains articles on many of the points above.

Software and code

Policy information about [availability of computer code](#)

Data collection

N/A

Data analysis

The energy expenditure data generated by the indirect calorimetry experiment were analyzed using two methods: 1. the NIDDK Mouse Metabolic Phenotyping Centers using their energy expenditure analysis page (<http://www.mmpc.org/shared/regression.aspx>) and 2. the R programming language with CalR, a custom package for analysis of indirect calorimetry using analysis of covariance with a graphical user interface (<https://calr.bwh.harvard.edu>)

The single cell RNA sequencing data were analyzed using several open source software packages, as described in detail with links to the source code in the methods section.

-Drop-seq sequencing data were processed into a digital gene expression matrix using the dropSeqPipe (<https://github.com/Hoohm/dropSeqPipe>) SnakeMake wrapper for Drop-seq tools version 1.13.

-The Seurat R package (version 2.3.1; <https://github.com/satijalab/seurat>) was used to project all sequenced cells onto two dimensions using t-Distributed Stochastic Neighbor Embedding (tSNE) and shared nearest neighbor graph-based clustering⁵⁷ was used to define clusters.

-The R programming language was used to analyze differential gene expression with Wilcoxon Rank Sum Testing

All other data were analyzed for statistical significance using GraphPad Prism v8.2.0

For manuscripts utilizing custom algorithms or software that are central to the research but not yet described in published literature, software must be made available to editors/reviewers. We strongly encourage code deposition in a community repository (e.g. GitHub). See the Nature Research [guidelines for submitting code & software](#) for further information.

Data

Policy information about [availability of data](#)

All manuscripts must include a [data availability statement](#). This statement should provide the following information, where applicable:

- Accession codes, unique identifiers, or web links for publicly available datasets
- A list of figures that have associated raw data
- A description of any restrictions on data availability

We deposited the single-cell RNA sequencing data in the NCBI Gene Expression Omnibus. Its accession number is GSE119960.

Field-specific reporting

Please select the one below that is the best fit for your research. If you are not sure, read the appropriate sections before making your selection.

Life sciences Behavioural & social sciences Ecological, evolutionary & environmental sciences

For a reference copy of the document with all sections, see nature.com/documents/nr-reporting-summary-flat.pdf

Life sciences study design

All studies must disclose on these points even when the disclosure is negative.

Sample size	Sample sizes were determined by doing a sample size estimate based on the differences and variability seen in data collected during preliminary pilot studies. We chose an alpha value of 0.05 and a beta value of 0.2 for these calculations.
Data exclusions	No data were excluded
Replication	The data in this manuscript were obtained from two groups (UCLA and AstraZeneca). The two lines of IDOL knockout mice were made independently, maintained in different vivariums on different continents. The robust IDOL knockout phenotype observed despite these factors speaks to the reproducibility of the results.
Randomization	Mice were randomly assigned to cages at weaning and the cages were allocated to experimental groups based on the sample size estimates.
Blinding	The studies were conducted without any notation on the cages of which mouse belonged which genetic group. The data were unblinded for analysis.

Reporting for specific materials, systems and methods

We require information from authors about some types of materials, experimental systems and methods used in many studies. Here, indicate whether each material, system or method listed is relevant to your study. If you are not sure if a list item applies to your research, read the appropriate section before selecting a response.

Materials & experimental systems

n/a	Involved in the study
<input type="checkbox"/>	<input checked="" type="checkbox"/> Antibodies
<input checked="" type="checkbox"/>	<input type="checkbox"/> Eukaryotic cell lines
<input checked="" type="checkbox"/>	<input type="checkbox"/> Palaeontology
<input type="checkbox"/>	<input checked="" type="checkbox"/> Animals and other organisms
<input checked="" type="checkbox"/>	<input type="checkbox"/> Human research participants
<input type="checkbox"/>	<input checked="" type="checkbox"/> Clinical data

Methods

n/a	Involved in the study
<input checked="" type="checkbox"/>	<input type="checkbox"/> ChIP-seq
<input checked="" type="checkbox"/>	<input type="checkbox"/> Flow cytometry
<input checked="" type="checkbox"/>	<input type="checkbox"/> MRI-based neuroimaging

Antibodies

Antibodies used

Rabbit anti VLDLR - ProteinTech #19493-1
 Rabbit anti-LDLR - Cayman Chemicals #1007665
 Mouse anti-Tyrosine Hydroxylase - Millipore #MAB318
 Rabbit anti-Phospho-HSL(Ser660) - Cell Signaling Technologies #4126
 Rabbit anti-HSL - Cell Signaling Technologies #4107
 Rabbit anti-GAPDH - ProSci #3781
 Rabbit anti-Actin - Sigma #A2066

Validation

The LDLR and VLDLR antibodies were validated using protein extracts obtained from knockout mice lacking the appropriate gene. The Tyrosine Hydroxylase antibody has been extensively validated by Fischer et al (DOI: 10.1038/nm.4316). The Phospho-HSL(Ser660) antibody was validated by the manufacturer by Western blot analysis of extracts from differentiated

NIH/3T3-L1 cells treated with isoproterenol
The HSL antibody was validated by the manufacturer by Western blot analysis of extracts from NIH/3T3 and differentiated 3T3-L1 cells
The GAPDH antibody was validated by the manufacturer by Western blot analysis of extracts from NIH/3T3 and 3T3-L1 cells
The Actin antibody was validated by the manufacturer by doing a Western blot titer analysis on Chicken Gizzard Extract on the affinity isolated purified antibody

Animals and other organisms

Policy information about [studies involving animals](#); [ARRIVE guidelines](#) recommended for reporting animal research

Laboratory animals	For all studies, male mice were used. The diets were initiated when the mice were 5-8 weeks old, as indicated in the appropriate figure legend. Mouse Strains: C57BL6/J (JAX #000664) VE Cadherin Cre (JAX #006317) Albumin Cre (JAX #003574) Mck Cre (JAX #006475) Villin Cre (JAX #004586) Adiponectin Cre (JAX #028020) Synapsin Cre (JAX #003966) Rosa26 Cre (AstraZeneca) IDOL knockout (UCLA - Peter Tontonoz's Laboratory) Idol fl/fl (UCLA - Peter Tontonoz's Laboratory) Idol fl/fl (AstraZeneca) VDLDR knockout (JAX #002529) LDLR knockout (JAX #002207)
Wild animals	N/A
Field-collected samples	N/A
Ethics oversight	The mouse studies conducted at UCLA were reviewed and approved by the Chancellor's Animal Research Committee (DHHS OLAW #A3196-01, UCLA approvals #99-131 and #03-166). The mouse studied conducted by AstraZeneca were approved by Gothenburg Ethics Committee for Experimental Animals, license nr: 38-2011.

Note that full information on the approval of the study protocol must also be provided in the manuscript.